microorganisms

MDPI

Article

Methylotenera-Driven Denitrification for Efficient Nitrogen Removal During Start-Up of a Mobile Dredged Residual Water Treatment Platform

Jiayin Huang [1,2], Yao Huang [1,*], Jinjin Ti [1], Pan He [2], Jiejun Zhao [2], Hao Zhang [2], Weimin Zhang [2], Gege Mei [1], Mengjuan Luo [1], Rong Li [1], Wen Cheng [1], Baoan Hu [2] and Hui Liu [1,*]

[1] School of Environmental Studies, China University of Geosciences, Wuhan 430078, China
[2] CCCC (Tianjin) Eco-Environmental Protection Design & Research Institute Co., Ltd., Tianjin 300202, China
* Correspondence: huangyao@cug.edu.cn (Y.H.); hliu2009@cug.edu.cn (H.L.)

Abstract

Mobile integrated platforms, represented by the "Light of Taihu Lake", are promising for treating dredged residual water, but the microbial mechanisms of nitrogen removal and their responses to operation parameters during start-up remain unclear. In this study, a 26-day start-up period divided into 8 operation stages was investigated using water quality monitoring, qPCR, 16S rRNA sequencing, Functional Annotation of Prokaryotic Taxa (FAPROTAX) prediction, fluorescence staining and metagenomics. Under a low influent C/N ratio (average 1.47), the platform achieved stable nitrogen removal (95.6% NH_4^+-N and 83.8% TN). Microbial analysis revealed a four-step directional succession, in which *Methylotenera* increased from <1% to 34%, becoming the most abundant classified genus. Respiratory activity was the most sensitive to process disturbances, whereas membrane integrity, metabolic activity and DNA integrity remained relatively high. PAM dosing and carbon source type were the major drivers of community structure, and *Methylotenera* cooperated with *Ellin6067* and *Terrimonas* for nitrogen removal. Metagenomic analysis showed that methylotrophic denitrification coupled with carbon–nitrogen metabolism was the core nitrogen removal pathway, while a multi-source nitrogen acquisition network supported nitrogen preservation. These findings advance understanding of microbial adaptation to low C/N ratio environments and provide a theoretical basis for regulation of integrated mobile dredged residual water treatment platforms.

Keywords: dredged residual water treatment; microbial community structure; methylotrophic denitrification; metabolic pathway; cell activity

Check for updates

Received: 27 October 2026
Revised: 23 November 2026
Accepted: 23 November 2026
Published: 27 November 2026

Copyright: © 2026 by the authors. Licensee MDPI, Basel, Switzerland. This article is an open access article distributed under the terms and conditions of the Creative Commons Attribution (CC BY) license.

1. Introduction

Dredging is an effective measure to reduce internal pollution and restore the aquatic ecological functions of rivers, lakes and reservoirs, which is significant for comprehensive water environment management [1,2]. Over 200 million m^3 of dredged mud-water mixtures are generated annually in European waterways [3,4], while in China, dredging projects in urban rivers and lakes produce more than 70 million tons of dredged sediments annually [5]. Wet dredging is currently the most widely used method, which generates huge amounts of high-moisture sediments and the subsequent dewatering process produces large volumes of residual water [6,7]. Current research mainly focuses on improving the dewatering efficiency of dredged sediments, including chemical flocculation [5,8] and mechanical de-

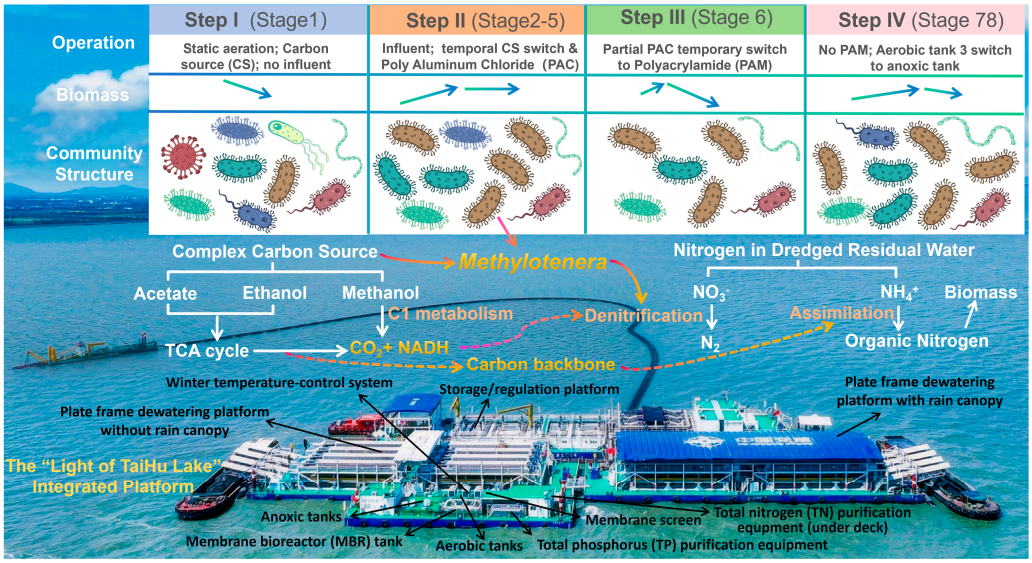
watering technical routes [9,10]. However, the residual water generated during dewatering and its treatment have received markedly insufficient attention.

Dredged residual water contains large amounts of particulate suspended solids and promotes the migration of pollutants (organic matter, nutrients, heavy metals, VOCs) into the aqueous phase during dewatering [7,8]. Improper discharge can cause secondary pollution of receiving water bodies [11–13]. For eutrophic water bodies where intensive dredging projects are normally applied, nutrient elements like nitrogen are a major concern. For example, despite two decades of high-intensity remediation projects, the annual average total nitrogen (TN) for Taihu Lake decreased from 3.71 mg/L in 2006 significantly to 1.56 mg/L in 2025 [14]. However, the present value is still higher than the required standard. As a large nutrient pool, sediment can contain much higher nitrogen concentrations and release nitrogen to porewater [15], increasing the nitrogen pollution risk of the residual water. In this study, the dredged residual water had average NH_4^+-N and TN concentrations of 3.78 ± 1.40 and 5.07 ± 1.75 mg/L, respectively (see details in Section 3.1). In recent years, regulatory authorities in most regions of China require residual water discharge to meet the Class III standard for lakes and reservoirs (GB 3838-2002) [16] (TN ≤ 1.0 mg/L, NH_4^+-N ≤ 1.0 mg/L), and some key watersheds like Taihu Lake have stricter local standards (DB32/1072-2018) [17]. Therefore, developing efficient and stable nitrogen treatment technologies for dredging residual water remains a common challenge.

For residual water treatment, a few studies have explored flocculant application. Lu et al. achieved rapid dewatering and residual water treatment via flocculant conditioning combined with geotextile tube filtration, improving water quality to meet discharge standards [5,7]. Li adopted an integrated magnetic flocculation-horizontal tube sedimentation process for treating dredging residual water from environmental restoration of Wolong Lake [18]. However, these physicochemical methods pay little attention to the removal of dissolved nutrients such as nitrogen. Thus, biochemical treatment units as standard protocols are still needed in practical engineering. Traditional immobilized water treatment systems have limitations such as large land occupation and the risk of secondary pollution. To address this, an integrated, mobile water treatment platform that enables screening, conditioning, dewatering, and biochemical treatment is needed in practice. A representative engineering example is the shipborne "Light of Taihu Lake" platform, which treats dredged residual water through a membrane screen, a multi-stage activated-sludge unit (aerobic and anoxic tanks in series), a vibrating membrane bioreactor (vMBR) for solid–liquid separation and sludge retention, and a downstream water-quality assurance unit for chemical phosphorus removal and post-denitrification. Sludge is returned to the aerobic tanks, and the treated effluent is intended to meet Class III surface-water standards [19]. However, the specific microbial mechanisms underlying nitrogen removal remain unclear.

Compared with chemical flocculation and dewatering, biological treatment of dredged residual water has received much less research attention. Direct reports on biochemical nitrogen removal from dredged residual water are scarce. The quality of dredged residual water varies considerably with dredging site, sediment properties, dewatering process and external inputs [7,8], which poses a challenge for biochemical treatment. Meanwhile, shipborne mobile platforms face unique challenges including constrained tank layout and hydraulic conditions due to limited space and vessel motion [20,21], as well as wave- and motion-induced shear and fluctuating mixing that can alter floc size distribution and settleability [22], therefore affecting pollutant removal. These disturbances differ fundamentally from the relatively stable conditions of fixed systems. Therefore, necessary process adjustments such as carbon source and flocculant dosing and types are required to achieve satisfactory effluent quality, especially during the start-up phase. Yet the directional succession of microbial communities and their functional and physiological responses are poorly

understood. Addressing these gaps is essential to understanding how mobile platforms achieve rapid start-up and stable nitrogen removal.



16S rRNA sequencing and metagenomics have been widely applied to wastewater treatment systems to resolve community succession and carbon/nitrogen metabolic pathways [15,23,24]. Fluorescence staining has also been applied to activated sludge to assess cell membrane integrity and viability to reflect cellular physiological state changes [25–27]. However, these approaches have rarely been combined to link community succession, functional gene dynamics, and physiological state under the dynamic operational disturbances typical of shipborne mobile platforms during start-up. In this study, therefore, water quality analysis, 16S rRNA sequencing, metagenomic functional gene detection, and multi-parameter fluorescence staining were combined to investigate microbial community succession and functional responses on the "Light of Taihu Lake" platform during ambient-temperature start-up. The objectives were to reveal the directional succession patterns of microbial communities and their physiological activity responses towards key process operations during start-up and to elucidate the nitrogen removal mechanism at the molecular level. The results are expected to provide a theoretical basis and technical support for the rapid start-up and precise regulation of mobile residual water treatment platforms.

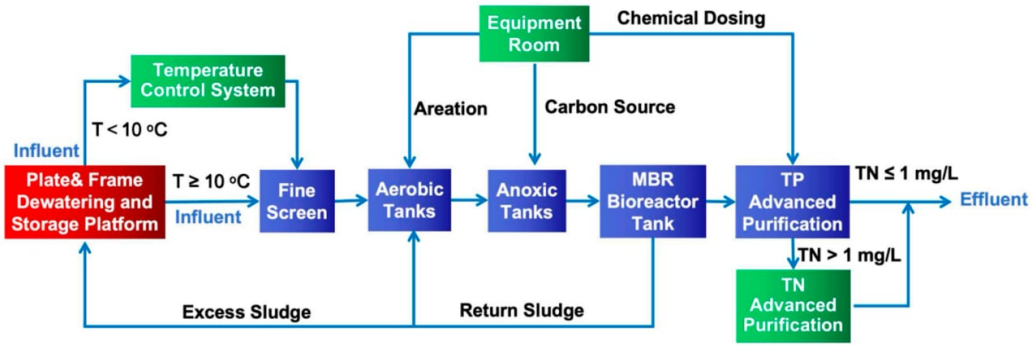
2. Materials and Methods

2.1. Platform Configuration

This study was conducted on the "Light of Taihu Lake" integrated residual water treatment platform (a shipborne mobile system) with a designed treatment capacity of 1000 m^3/d, a minimum design temperature of 4 °C, a total rated power of 252 kW and a total weight of 600 t. The platform adopts multi-stage activated sludge biochemical tanks combined with vMBR and an enhanced nitrogen and phosphorus removal process. Scheme 1 shows the simplified process flow diagram displaying the main biochemical unit.

After a membrane screen removes particulate suspended solids, the influent enters the main biochemical unit, consisting of three aerobic tanks (Tank 1 to 3) and three anoxic tanks (Tank 4 to 6) connected in series. The following vMBR tank achieves efficient solid–liquid separation, maintains a high sludge concentration in the system, and returns sludge to the aerobic tanks to ensure stable operation of the biochemical system. After the MBR membrane tank, a water quality assurance system is installed, including a chemical phosphorus removal

unit (with phosphorus removal agent dosing) and a post-denitrification unit, to reduce total phosphorus and total nitrogen further and ensure effluent indicators consistently meet the Class III surface water standard throughout the year. Excess sludge generated by the system is periodically discharged to the front-end slurry conditioning tank, mixed with the original dredged slurry, and then uniformly dewatered by a plate-and-frame filter press. The filter cake is transported off-site for disposal, and the filtrate is returned to the front end of the system for reprocessing.



Scheme 1. Process flow diagram of the residual water treatment.

2.2. Start-Up Operation and Process Parameters

The present research was conducted from 29 July to 23 August, 2025 (26 days total) during the start-up phase, with an average influent temperature of 31.6 °C. The targeted dredged residual water was generated from the ecological dredging project in Meiliang Bay, Taihu Lake. It originated from the filtrate obtained after the sediment slurry was transported by a high-concentration micro-disturbance cutter suction dredger to the "Light of Taihu Lake" plate-and-frame filter-pressing dewatering platforms. It then underwent vibratory screening, sediment conditioning, and plate-and-frame filter-pressing dewatering at a pressing pressure of 0.8 MPa for 45–60 min.

The initial activated sludge was obtained from the aerobic tank of an A^2/O process at a municipal wastewater treatment plant in Wuxi city, China. The initial inoculation volume of activated sludge was 150 m^3, which was added to the aerobic tank in a single batch. The average mixed liquor suspended solids (MLSS) concentration was approximately 3000 mg/L, and the sludge was yellow-brown in color. After static aeration, the 30 min sludge settling ratios (SV_{30}) of anoxic tank 6 and the membrane tank were 24% and 22%, respectively, with corresponding sludge volume indices (SVI) of 80 and 73 mL/g, indicating good sludge settling performance.

The influent flow rate was kept at 36 m^3/h (864 m^3/d). The hydraulic retention time (HRT) in the aerobic and anoxic tanks was approximately 3.5 h and 6 h, respectively. During operation, the dissolved oxygen (DO) in the aerobic tanks was maintained at 2.0–3.0 mg/L, and the DO in the anoxic tanks was <0.1 mg/L. The average oxidation-reduction potential (ORP) in the anoxic tanks was −169 mV.

During start-up, sludge acclimation, conditioning agent dosing (such as carbon sources, PAC and PAM), and process parameter adjustments (such as carbon source type switching and aeration intensity regulation) were implemented. NH_4Cl was added only during Stage 1 (29 July–2 August) under static aeration, as a maintenance nitrogen source to prevent endogenous decay and preserve the functional potential of the inoculated sludge before continuous influent began. Carbon sources were dosed in anoxic tank 2, and flocculant agents were dosed in anoxic tank 4. The sludge return ratio was set at 350%. The specific division of operational stages and operating parameters is detailed in Table 1. The specific

dosing dosages are shown in Figure S1. Chemicals were dosed as stock solutions on a daily volumetric or mass basis (L or kg) according to the metering-pump settings, and each chemical was added within an 8 h window (08:00–16:00) each day. Excess sludge was discharged only once during the entire start-up period, on the afternoon of 20 August. The waste sludge volume was determined by multiplying the MBR tank surface area by the water-level drop before and after sludge wasting, and was 12 m^3.

Table 1. Specific process stages of residual water biochemical treatment.

Date	Stage	Process Adjustments
7.29–8.2	1	Static aeration
8.3–8.5	2	Continuous influent started; Carbon source 1
8.6	3	Continuous influent; Carbon source 1 + PAC; sludge return
8.7–8.8	4	Continuous influent; Carbon source 2 + PAC; sludge return
8.9–8.10	5	Continuous influent; Carbon source 1 + PAC; sludge return
8.11–8.15	6	Continuous influent; Carbon source 1 + PAC + PAM; sludge return
8.16–8.18	7	Continuous influent; Carbon source 1 + PAC; sludge return
8.19–8.23	8	Aerobic tank 3 converted to anoxic; continuous influent; Carbon source 1 + PAC

The carbon source and conditioning agents dosed during operation were all purchased from Hongfeng Chemical Co., Ltd. (Changzhou, China). Carbon source 1, a commercial high-efficiency composite liquid carbon source (mainly composed of sodium acetate, methanol, and ethanol), with equivalent COD of 300,000 mg/L and an effective component content ≥90%. Carbon source 2, a sodium acetate solution, with a COD equivalent of 200,000 mg/L and purity ≥99%. Polyaluminum chloride (PAC) (industrial grade, with $Al_2O_3 \geq 28\%$) was prepared as a 10 wt% aqueous solution before use. Cationic polyacrylamide (PAM) (molecular weight 8–12 million, effective component content ≥90%) was prepared as a 1 wt‰ aqueous solution before use. Ammonium chloride was of industrial grade with purity ≥99.0%.

2.3. Water Quality Monitoring

Water-quality monitoring started on 5 August (late Stage 2) when continuous influent started. Water quality indicators (COD, ammonia nitrogen, total nitrogen, total phosphorus, and pH) were automatically monitored using a C310 online automatic water quality monitor (Bescient Technologies Co., Ltd., Shenzhen, China) via spectrophotometry. The instrument automatically updates and stores its measurements every 2 h. Effluent turbidity was measured using a TC-NTU2 turbidity meter (Beiyi Tongchuang Instrument Co., Ltd., Beijing, China) based on light scattering. Online monitoring of MLSS in the MBR tank was performed with a sludge concentration sensor (Beiyi Tongchuang Instrument Co., Ltd., Beijing, China). Influent, effluent and MLSS data were collected twice daily, in the morning (8 a.m.) and afternoon (4 p.m.). Each reading represents the instrument-reported value at the time of recording, rather than a replicate measurement of the same sample or a time-window average. Water temperature was recorded with a portable temperature meter at the corresponding time. Summary statistics reported regarding data range and mean ± SD were calculated from recorded readings over 5 August to 23 August ($n = 36$) and therefore represent the overall variability across the start-up period. In contrast, for temporal dynamic plots, the twice-daily readings are treated as sequential individual observations rather than averaged.

In addition, suspended solids (SS), alkalinity and total salinity of the influent were determined on collected samples according to standard methods. SS was measured by the

gravimetric method after filtration through a 0.45 μm membrane and drying at 103–105 °C to constant weight (GB/T 11901-1989) [28]. Alkalinity was determined by acid–base titration with standardized sulfuric acid to the phenolphthalein and methyl orange endpoints. Total alkalinity was expressed as mg/L as $CaCO_3$ (acid–base indicator titration, GB/T 15451-2006/Standard Methods) [29]. Total salinity was measured by the gravimetric method after evaporation and drying of a filtered sample at 105 ± 2 °C (HJ/T 51-2024) [30]. These statistical data were reported as range and average data with SD ($n = 9$).

2.4. Sludge Sampling and Microbial Analysis

Sludge sampling was conducted from Stage 1 to 8. From 29 July to 4 August, only anoxic tank sludge samples were collected daily at 4:00 p.m. From 5 August onward, sludge samples were collected daily from both the aerobic and anoxic tanks. These samples with a total of 45 samples were denoted as TH + date + HY/QY, where HY and QY stand for aerobic tank and anoxic tank, respectively. A bailer sampler equipped with a 1.5 m extension rod, 500 mL polypropylene sampling bottles, disposable protective gloves, and a deionized water rinse bottle was used for sludge sampling. Before and after sampling, the sampling tools were rinsed with tap water and deionized water to avoid cross-contamination. Samples were collected at approximately 0.5 m below the liquid surface of each tank. Influent and effluent sampling points were located before the membrane screen and at the product water tank, respectively.

After returning the sludge-water mixture to the laboratory the same day, it was thoroughly mixed and divided into two aliquots. One aliquot was kept unfiltered at 4 °C in the dark and used for fluorescence analysis within 24 h. The other aliquot (100 mL) was vacuum-filtered through a 0.22 μm membrane to enrich microorganisms on the membrane surface. The membrane was then removed, placed in a sterile zip-lock bag, and stored at −80 °C until DNA extraction for sequencing, qPCR and metagenomic analysis.

2.4.1. DNA Extraction and 16S rRNA Sequencing

The above 45 sludge samples collected from Stages 1 to 8 were subjected to DNA extraction and 16S rRNA sequencing. DNA was extracted using a modified cetyltrimethylammonium bromide (CTAB) method and stored at −20 °C prior to further analysis. DNA quantity and quality were assessed using a NanoDropNC2000 spectrophotometer (Thermo Fisher Scientific, Waltham, MA, USA) and agarose gel electrophoresis, respectively. The V3–V4 region of the 16S rRNA gene was amplified using the primer pair 338F (5′-ACTCCTACGGGAGGCAGCA-3′) and 806R (5′-GGACTACHVGGGTWTCTAAT-3′). One no-template PCR control, in which sterile water replaced the DNA template, was included to monitor PCR-derived contamination and it yielded negligible reads.

Sequencing was performed by Personal Biotechnology Co., Ltd. (Shanghai, China) on the Illumina NovaSeq platform. A total of 3,398,653 raw reads were obtained with an average of 75,526 per sample. Sequences were then quality-filtered, denoised, merged, and chimera-removed using the DADA2 plugin with default parameters. After these steps, 2,127,874 high-quality reads were retained (mean 47,286 ± 7714 per sample, ranging from 32,55 to 67,404). Taxonomy was assigned to ASVs using the classify-sklearn naïve Bayes taxonomy classifier in the feature classifier plugin against the SILVA Release 138 Database. The taxonomic compositions and abundances were visualized using MEGAN and GraPhlAn. For genus-level composition, sequences that could not be classified at the genus level were excluded before relative abundance calculation, and the remaining classified genera were renormalized to 100%.

Bioinformatics analyses were mainly performed on the QIIME 2 platform and R packages (v4.3.3). Alpha diversity was assessed using Chao1 and Shannon indices calculated

based on the ASV/OTU table rarefied to 95% of the minimum sequencing depth across all samples. The results were expressed as descriptive statistics for the 45 samples individually, without statistical testing. Beta diversity analysis was performed using Bray–Curtis metrics and visualized via unweighted pair-group method with arithmetic means (UPGMA) hierarchical clustering and principal coordinate analysis (PCoA). For PCoA, samples were divided into four groups with at least five samples per group. 95% confidence ellipses were added and group differences were tested by PERMANOVA based on Bray–Curtis distances and visualized with boxplots. $p < 0.05$ was considered statistically significant. Potential metabolic functions of the bacterial communities were predicted using FAPROTAX. The ASV abundance table was collapsed to genus-level taxonomy, and functional annotations were assigned based on the manual curation of published literature.

2.4.2. Microbial Gene Quantification by Quantitative PCR

The DNA templates used for quantitative PCR (*q*PCR) were the DNA samples returned after 16S rRNA sequencing. *q*PCR was performed in a total reaction volume of 10 µL, consisting of 5 µL of PowerUp™ SYBR™ Green Master Mix (Applied Biosystems, Thermo Fisher Scientific, USA), 0.25 µL each of forward primer 314F (5′-CCTACGGGAGGCAGCAG-3′) and reverse primer 515R (5′-ATTACCGCGGCTGCTGGCA-3′), 1 µL of DNA template, and 3.5 µL of nuclease-free water. Each sample was run in three technical replicates.

The amplification program was carried out on a QuantStudio 3 real-time PCR system (Applied Biosystems, Thermo Fisher Scientific, Waltham, MA, USA) using a two-step protocol: initial denaturation at 95 °C for 2 min, followed by 40 cycles of 95 °C for 15 s and 60 °C for 1 min (annealing/extension), with fluorescence signal acquired at the end of the 60 °C step. After cycling, a melt curve analysis was performed: 95 °C for 15 s, 60 °C for 1 min, then ramping from 60 °C to 95 °C at a rate of 0.15 °C/s with continuous fluorescence acquisition to generate the melt curve, in order to verify the specificity of the amplification products. QuantStudio Design & Analysis Software v1.4.3 was used for analysis. For quantification, a standard curve was constructed using ten-fold serial dilutions of standards with known copy numbers. The gene copy numbers of the samples were then calculated from the Ct value and the standard curves.

2.4.3. Metagenomic Sequencing

Five representative samples were selected for metagenomic sequence analysis by Personal Biotechnology Co., Ltd. (Shanghai, China). The extracted microbial DNA was processed to construct metagenome shotgun sequencing libraries with an insert size of 400 bp using the Illumina TruSeq Nano DNA LT Library Preparation Kit. Each library was sequenced on an Illumina NovaSeq platform (Illumina, San Diego, CA, USA) with the PE150 strategy. Raw reads were quality-filtered by removing adapters and trimming low-quality reads using fastp (v 0.23.2). Valid reads from each sample were concatenated and assembled using MEGAHIT (version 1.1.2), with contigs ≥300 bp retained. These samples were selected to cover the initial, middle and late successional stages and to contrast aerobic and anoxic conditions. Because the pilot platform was operated as a single continuous flow system, independent biological replicates were not available at each time point.

Functional annotations were performed using MMseqs2 in search mode (parameter -s 5.7) against databases such as KEGG to obtain taxonomic and functional abundance tables. Gene abundances were normalized to transcripts per million (TPM) to account for sequencing depth and gene length variation. The resulting TPM values represent the relative abundance of each KEGG ortholog (KO) category in each sample. Biogeochemical pathway annotation was conducted using DiTing v2.0, a KEGG-based pipeline for inferring biogeochemical pathways from metagenomic data. Genes were predicted with Prodigal

v2.6.3 and annotated against the KOfam database using KofamScan. Relative abundances of carbon and nitrogen cycling pathways were calculated using DiTing's built-in formulae, and pathway diagrams were generated from the output reports.

2.4.4. Microbial Activity Detection by Fluorescence Staining

All fluorescence staining procedures were performed within 24 h after sampling. Before staining, the sludge-water mixture was thoroughly vortexed and washed twice with PBS. Four fluorescent staining methods were used, and observations were performed on an FR-4A fluorescence microscope (Cossim, Shanghai, China) to evaluate cell membrane integrity rate, DNA integrity rate, metabolic activity, and respiratory activity, respectively. For all measurements, at least three individual fields of view were recorded and used for statistics, with averaged data reported. The specific staining methods are as follows.

Membrane integrity rate was determined using the SYTO9/propidium iodide (PI) double-staining method [27]. SYTO9 is a membrane-permeable green fluorescent dye that labels nucleic acids in all cells. At the same time, PI is a membrane-impermeable red fluorescent dye that can only enter dead cells with damaged membranes. That means live cells appear green and dead cells appear red. A 1 mL sample was placed in a centrifuge tube, and 1.5 µL SYTO9 (3.34 mM) and 1.5 µL PI (20 mM) were added. The mixture was vortexed and incubated at room temperature in the dark for 30 min. A 10 µL aliquot was placed on a glass slide and examined under G/B excitation. Image J 1.52i (Java 1.8.0_172) (NIH Image, Bethesda, MD) was used to segment colors and count cells. Membrane integrity rate was calculated as the ratio of green cells/(green + red cells).

DNA integrity rate was determined using the SYBR Green I/PI double-staining method [31]. SYBR Green I can penetrate intact cell membranes and bind to double-stranded DNA, emitting green fluorescence, while PI can only enter cells with damaged membranes and preferentially binds to fragmented DNA, emitting red fluorescence. Green cells represent intact DNA, while red cells represent DNA damage or membrane rupture. A 100 µL sample was mixed with 100 µL PI (5 µg/mL) and 10 µL SYBR Green I (10 µg/mL). The mixture was vortexed and incubated in the dark for 20 min. A 10 µL aliquot was examined under B excitation, and counting was performed as described above. DNA integrity rate was calculated as the ratio of green cells/(green + red cells).

Metabolic activity was determined using the FDA/PI double-staining method [32]. Nonpolar FDA (fluorescein diacetate) can freely diffuse across intact cell membranes and is hydrolyzed by endogenous esterases in metabolically active cells into polar fluorescein derivatives with green fluorescence, while PI selectively labels cells with damaged membranes and emits red fluorescence. A 1 mL sample was mixed with 4 µL FDA (10 mg/mL) and 5 µL PI (1 mg/mL) and then incubated in the dark for 30 min. After incubation, the mixture was centrifuged at 5000 r/min for 2 min. The supernatant was discarded, and the pellet was resuspended in PBS, washed twice, and finally resuspended in 1 mL PBS. A 10 µL aliquot was examined under B excitation. Metabolic activity rate was calculated as the ratio of green cells/(green + red cells).

Respiratory activity was determined using the CTC/DAPI double-staining method [33]. 5-cyano-2,3-ditolyl tetrazolium chloride (CTC) can freely enter intact cells and is reduced by active respiratory chain dehydrogenases to insoluble red fluorescent formazan precipitates. DAPI is a membrane-permeable DNA dye that binds to DNA in all cells and produces blue fluorescence. A 100 µL sample was mixed with 10 µL CTC (50 mM) and incubated in the dark for 2 h. Subsequently, 500 µL sterile water and 2.5 µL DAPI (1 µg/mL) were added, and the mixture was vortexed and allowed to stand for 30 min. A 10 µL aliquot was examined under G excitation for CTC and UV excitation for DAPI. Image J was used to split channels. Respiratory activity rate was calculated as the ratio of red cells/blue cells. For

this staining, if fewer than three countable fields were available in five attempts, the sample was recorded as missing and excluded from the trend analysis.

All chemicals for indoor experiments are of or above analytical grade. Fluorescent dyes including SYTO9 (green fluorescent nucleic acid stain), propidium iodide (PI), SYBR Green I (nucleic acid stain), fluorescein diacetate (FDA), 5-cyano-2,3-ditolyl tetrazolium chloride (CTC), and 4′,6-diamidino-2-phenylindole (DAPI) were purchased from Shanghai Jiqi Biotechnology Co., Ltd. (Shanghai, China). The other chemical reagents required for laboratory testing were purchased from Sinopharm Chemical Reagent Co., Ltd. (Shanghai, China).

3. Results and Discussion

3.1. Water Quality Characteristics of the Dredging Residual Water in the Present Work

This study was conducted on the "Light of Taihu Lake" platform. The influent in the present work was the dredged residual water generated from the ecological dredging project in Meiliang Bay, Taihu Lake, and was obtained as the filtrate after vibratory screening, sediment conditioning, and plate-and-frame filter-pressing dewatering. Table 2 summarizes the main water-quality characteristics during start-up stages 2–8. Stage 1 was a static-aeration acclimation period without continuous influent, so no water-quality data were recorded, and it was therefore excluded from the removal-efficiency calculation. Overall, the residual water showed low organic and nutrient concentrations (average COD 6.62 mg/L, NH_4^+-N 3.78 mg/L, TN 5.07 mg/L, and TP 0.0337 mg/L), a near-neutral pH (7.00), low SS (26 mg/L) and alkalinity (61.44 ± 18.93 mg/L as $CaCO_3$), and a relatively high total salinity (3366 mg/L). The average COD/TN ratio was determined to be 1.47, indicating a typical low C/N condition for biological nitrogen removal. As a limitation, other water quality indices such as major ions or heavy metals were not determined, as the engineering monitoring focused on dissolved nitrogen removal performance rather than comprehensive physical/chemical characterization.

Table 2. Major water quality indices of the dredging residual water.

Water Quality Index	Range	Average ± SD
Temperature (°C)	30.2–33.7	31.6 ± 0.9
COD (mg/L) [a]	2.68–9.68	6.62 ± 1.41
NH_4^+-N (mg/L) [a]	0.10–5.46	3.78 ± 1.40
TN (mg/L) [a]	0.20–7.38	5.07 ± 1.75
TP (mg/L) [a]	0.01–0.18	0.0337 ± 0.0123
pH [a]	6.18–7.40	7.00 ± 0.25
SS (mg/L) [b]	11.0–53.0	26.0 ± 13.4
Alkalinity (mg/L as $CaCO_3$) [b]	20.0–77.0	61.4 ± 18.9
Total salinity (mg/L) [b]	2450–6260	3366 ± 1123

[a.] Statistical results were based on the automatic monitoring results (n = 36). [b.] Statistical results were based on measurements of collected influent samples (n = 9).

3.2. Nitrogen Removal Performance of the Platform During Start-Up

During Stages 2–8, the platform underwent 8 process adjustment stages during the ambient-temperature start-up, as shown in Table 1. Automatic water quality monitoring showed that average influent COD was 6.62 ± 1.41 mg/L, while average effluent COD increased to 8.28 ± 1.71 mg/L. Nevertheless, the effluent COD still remained relatively low. The average influent TP was 0.0337 ± 0.0123 mg/L, which increased to 0.091 ± 0.049 mg/L in the effluent. The average influent NH_4^+-N was 3.88 ± 1.25 mg/L, which decreased to 0.139 ± 0.049 mg/L in the effluent. The average influent TN was 5.20 ± 1.58 mg/L, which

decreased to 0.757 ± 1.03 mg/L in the effluent. The average pH increased from 7.00 ±0.25 to 7.20 ± 0.24. The average removal efficiencies for NH_4^+-N and TN were 95.6% and 83.8%, respectively. These data were calculated for each monitoring time point, and the reported value was the mean of all time-point efficiencies during Stages 2–8.

Figure 1a,b further illustrate the temporal trends of influent and effluent TN and NH_4^+-N for the continuous-flow period in Stages 2–8 (from 5 to 23 August) during start-up. Influent TN and NH_4^+-N fluctuated within 0–8 mg/L and 0–6 mg/L, respectively, with generally consistent trends. Effluent TN remained at a low level (<1 mg/L) during stages 2–3, but increased rapidly to approximately 4.5 mg/L in stage 4 when carbon source 1 was switched to carbon source 2, and then decreased in stage 5 when carbon source 2 was switched back to 1. This phenomenon indicates that carbon source 2 (pure sodium acetate) impairs the denitrification function of the system. In the middle of Stage 6, effluent TN slightly increased to 1 mg/L and then decreased, possibly related to PAM dosing. In Stage 7, effluent TN again transiently increased to approximately 4.5 mg/L and then decreased, possibly related to the increased PAC dosage. In Stage 8, TN initially increased slightly and then rapidly decreased, stabilizing at approximately 0.2 mg/L, indicating that converting the aeration tank to an anoxic tank improved TN removal. Regarding NH_4^+-N removal, effluent NH_4^+-N remained stable at approximately 0.1 mg/L throughout the start-up process, indicating that the nitrification function of the system was relatively stable. Only at the end of stage 6 did effluent NH_4^+-N show a transient slight rebound, which may be due to the decomposition of amide groups on PAM molecules releasing NH_4^+-N under microbial or chemical action [34]. Overall, the system exhibited satisfactory TN and NH_4^+-N removal performance during ambient-temperature start-up, although its removal capacity showed occasional fluctuations in certain stages.

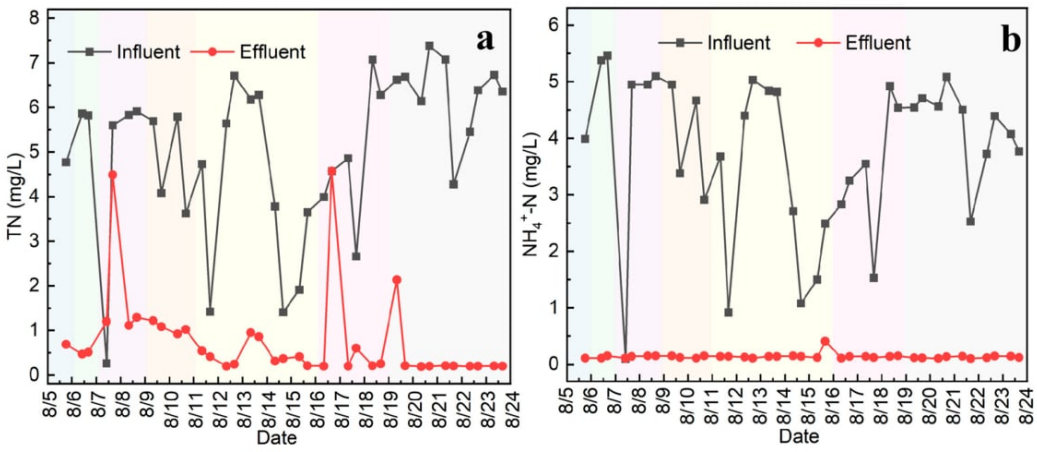


Figure 1. Total nitrogen (**a**) and ammonia nitrogen (NH_4^+-N) concentrations (**b**) in the influent and effluent for the continuous-flow period in Stages 2–8 of start-up. Data are individual instrument-reported readings at 8:00 a.m. and 4:00 p.m. every day and therefore plotted as sequential observations without error bars shown.

In addition to nitrogen, the dynamics of COD, TP, pH and turbidity are provided in Figure S2. In Stages 2–5, effluent COD gradually increased and frequently exceeded influent COD, indicating carbon slip from external carbon source dosing. After the reduction of carbon source dosage from Stage 6, effluent COD began to decrease and finally approached the influent level in late Stage 8. Effluent TP was mostly higher than influent TP from Stage 2 (indicating endogenous release and/or phosphorus impurities), declined transiently in Stage 3 (due to PAC flocculation), peaked at ~0.65 mg/L in 7 August (Stage 4, when PAC addition stopped) and returned to low levels after PAC dosing recovered, fluctuated again in

Stage 6 (when PAC dosages were temporarily reduced) and remained relatively low in late Stage 7 to Stage 8. Overall, TP removal was dominated by PAC dosing and the contribution of biological phosphorus removal was limited. Effluent pH was mostly ~7.2, with transient acidification to ~6.2 during PAC dosing in Stages 3–4 (likely due to Al^{3+} release from PAC hydrolysis), and later remained higher than influent pH, possibly due to denitrification alkalinity and CO_2 stripping due to aeration. Turbidity remained generally below 1.5 NTU, fluctuating only in Stage 8, likely associated with the conversion of aerobic tank 3 to anoxic conditions and the resulting adjustment of floc structure.

During Stages 2–8, MLSS in MBR tanks increased from approximately 5000 to 20,000 mg/L, indicating substantial net solids accumulation. This possibly suggested an increase in biomass during the start-up. However, MLSS also included inorganic solids derived from PAC dosing and influent suspended solids and was strongly affected by membrane retention and sludge return. It is therefore used here only as qualitative evidence of net solids accumulation and could not be directly converted into a quantitative estimate of bacterial biomass.

A semi-quantitative nitrogen balance was constructed for the continuous-flow period in Stages 2–8 (from 5 to 23 August) to assess the fate of the removed nitrogen. The influent TN load was estimated from the daily flow rate (864 m^3/d), the 18-day duration and the measured average influent TN concentration to be 80.87 kg N. The nitrogen input from PAM was estimated from its nitrogen content and the recorded total dose (of the 1‰ wt stock solution), corresponding to about 0.04 kg N, less than 0.1% of the influent TN load. Carbon source and PAC were assumed to contain no nitrogen, so both were neglected from TN input. Biological nitrogen fixation was not quantified. The fate of influent TN can be summarized as [35]: (1) effluent TN, (2) nitrogen discharged with excess sludge, (3) nitrogen accumulated in the system and (4) gaseous nitrogen loss (including denitrification, with minor ammonia volatilization and possible anammox). Among them, Effluent TN loads were calculated based on the average effluent TN concentration to be 11.77 kg N, accounting for 14.6% of the influent TN load. The nitrogen discharged with excess sludge was estimated from the single discharge event on 20 August (12 m^3 at MLSS of 19,597 mg/L), assuming a VSS/SS ratio of 0.7 and a biomass nitrogen content of 0.10 g N/g VSS [36], which gave approximately 16.46 kg N (20.4% of the influent TN load). The remaining 52.64 kg N (65.1% of the influent TN load) represents the sum of gaseous nitrogen loss and nitrogen accumulated in the system biomass. These two terms could not be separated, because N_2/N_2O fluxes and ammonia volatilization were not measured and the system accumulation term could not be reliably quantified. The balance is therefore explicitly stated as semi-quantitative.

3.3. Changes in Microbial Community Structure

To evaluate the trend of total biomass during start-up, absolute quantification of the 16S rRNA gene was performed using *q*PCR, and the results are shown in Figure 2a. In Stage 1, the 16S rRNA gene copy number decreased from an initial value of approximately 3×10^7 to 2.2×10^7 copies/mL after a transient increase, indicating that the inoculated sludge experienced an adaptation period after entering a new environment. After continuous influent was started in Stage 2, the total copy number rose to 4.2×10^7 copies/mL, indicating that carbon source dosing effectively drove microbial proliferation. During Stages 3–5, the total copy number fluctuated between 3.5×10^7 and 4.5×10^7 copies/mL. During PAM dosing in Stage 6, the total copy number initially decreased to 3.5×10^7 copies/mL, then increased to 4.8×10^7 copies/mL, and subsequently decreased to 2.0×10^7 copies/mL (at the end of Stage 6), suggesting that PAM may initially enrich bacterial cells through flocculation, but continuous exposure led to a net loss of biomass. In Stage 7, the total copy number

fluctuated between 1.8×10^7 and 2.5×10^7 copies/mL. After the anoxic conversion in Stage 8, the total copy number first rebounded to 3.2×10^7 copies/mL and then slightly decreased to 2.5×10^7 copies/mL, indicating that anoxic conditions inhibited total population growth. Overall, the absolute abundance of total bacteria in the aerobic and anoxic tanks showed generally consistent trends, with differences within an order of magnitude.

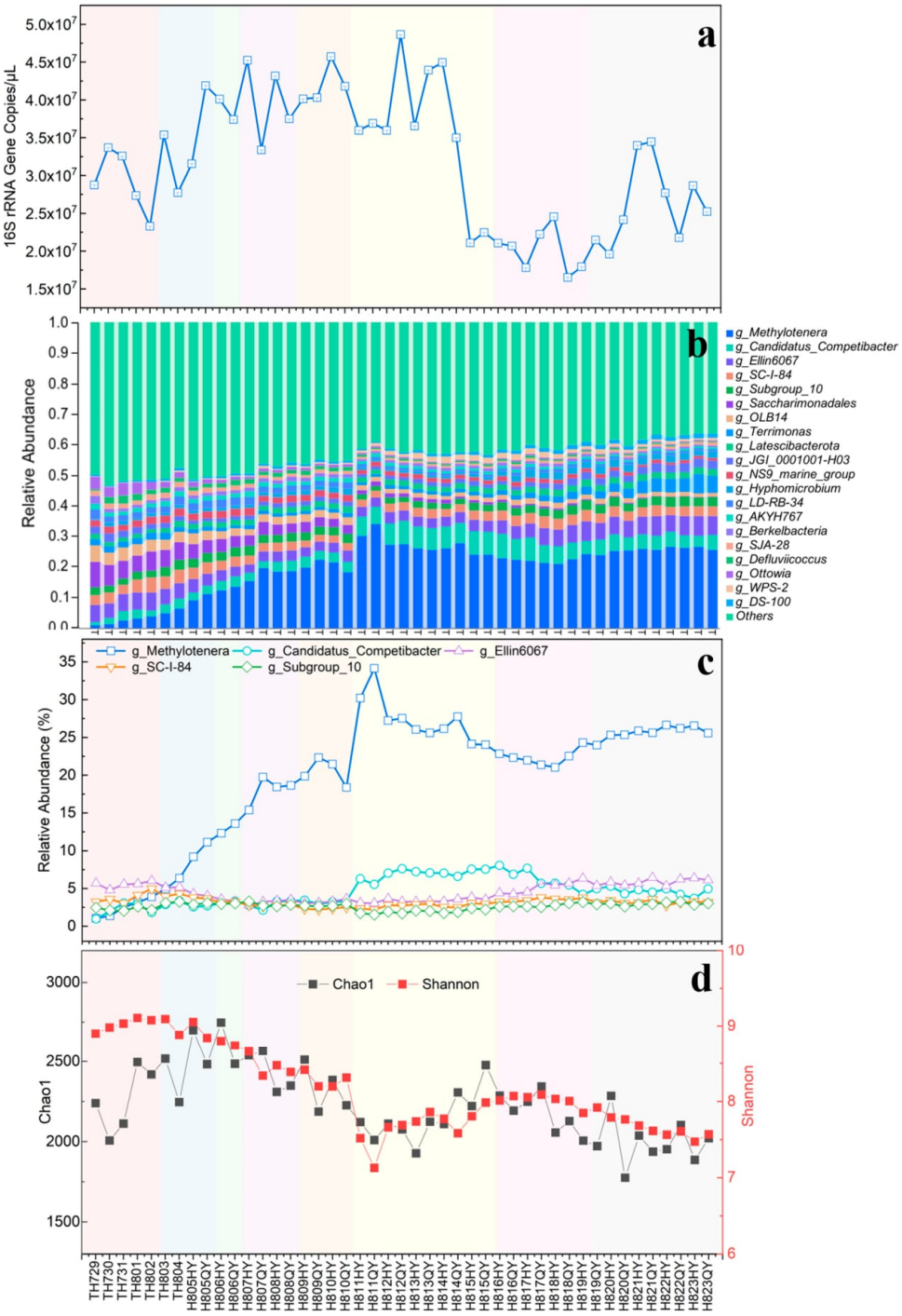


Figure 2. Absolute 16S rRNA gene abundance (**a**), microbial community composition at the genus level (top 20) (**b**), temporal changes in the top 5 abundant classified genera (**c**), and changes in alpha diversity indices (**d**) during start-up. Relative abundances in (**b**) were calculated excluding sequences unclassified at the genus level. "Others" comprises classified genera outside the top 20 in abundance.

To investigate the response and succession patterns of the microbial community during start-up, 16S high-throughput sequencing was used to analyze the microbial community structure in the aerobic and anoxic tanks. Figure 2b showed the microbial community composition at the genus level, with the top 20 most abundant genera displayed. It could be inferred that the top five abundant classified genera during start-up were *Methylotenera*, *Candidatus Competibacter*, *Ellin6067*, *SC-I-84* and *Subgroup_10*. *Methylotenera* is a methylotrophic bacterium that can utilize one-carbon compounds such as methanol and methylamine and perform denitrification [37]. *Candidatus Competibacter* is a glycogen-accumulating organism (GAO) involved in endogenous denitrification [38] and possesses incomplete denitrification capacity for reducing nitrate to nitrite [39]. *Ellin6067* is an ammonia-oxidizing bacterium (AOB) widely distributed in nature and wastewater treatment systems, participating in the first half of nitrification [40]. SC-I-84 also possesses incomplete denitrification capacity and can reduce nitrate to nitrite [41]. *Subgroup_10* is a taxonomic group within the phylum *Acidobacteria*, a metabolically specialized bacterium that exclusively utilizes rhizosphere active organic carbon [42].

The temporal changes in the top five abundant classified genera are plotted in Figure 2c. At the beginning of system start-up, the abundance of *Methylotenera* was approximately 1% and increased only slightly in Stage 1. From Stage 2 to early Stage 4, its abundance gradually increased to 20%, indicating that continuous supply of No. 1 composite carbon source favored the enrichment of *Methylotenera*. However, in late Stage 4, its abundance slightly decreased, indicating that switching to carbon source 2 was unfavorable for *Methylotenera* enrichment. From Stage 5 to early Stage 6, the abundance of *Methylotenera* increased explosively to 34%. However, it then decreased significantly to approximately 20% from late Stage 6 to Stage 7, indicating that PAM dosing inhibited *Methylotenera* abundance. From late Stage 7 to Stage 8, *Methylotenera* abundance slowly recovered to approximately 27%. The abundance of *Candidatus Competibacter* was approximately 1% at Stage 1 and increased slightly to 2.5% in Stages 2- 5, increased significantly to 7% in Stage 6, and gradually decreased to 4% in Stages 7–8. *Ellin6067* had an initial abundance of 5%, decreased slightly from Stage 1 to 5, stabilized at approximately 3% in Stage 6, and recovered to approximately 6% in Stages 7–8. The abundances of *SC-I-84* and *Subgroup_10* changed little, remaining at approximately 3% and 2%, respectively.

Figure 2d shows the changes in the community diversity indices Chao1 and Shannon during start-up. Overall, both indices showed a gradual decline during start-up, indicating that under continuous selective pressure, species richness and evenness decreased and the community structure became simpler and more concentrated, with a few genera such as *Methylotenera* winning the competition and gradually becoming abundant.

To further analyze the β-diversity of the microbial community, hierarchical clustering analysis and principal coordinate analysis (PCoA) were performed based on Bray–Curtis distance. To obtain robust grouping, samples were first divided into eight groups, ST1–ST8, corresponding to the eight process adjustment stages in Table 1, and hierarchical clustering was performed at the genus level (Figure 3a). The branching order of the clustering tree showed that samples exhibited clear differentiation according to process adjustment stages, with a relatively continuous gradient change overall. All samples were first divided into two major branches: branch I (Stages 1–5) and branch II (Stages 6–8). Branch I was further divided into a single-sample cluster for Stage 1 and a mixed cluster for Stages 2–5. Branch II was divided into a single-sample cluster for Stage 6 and a mixed cluster for Stages 7–8. This result indicated that the most significant difference was between the early-to-middle start-up period (Stages 1–5) and the late start-up period (Stages 6–8). In the early-to-middle period, the community structure differed significantly between Stage 1 and Stages 2–5, and in the late period, the difference between Stage 6 and Stages 7–8 was also relatively obvious.

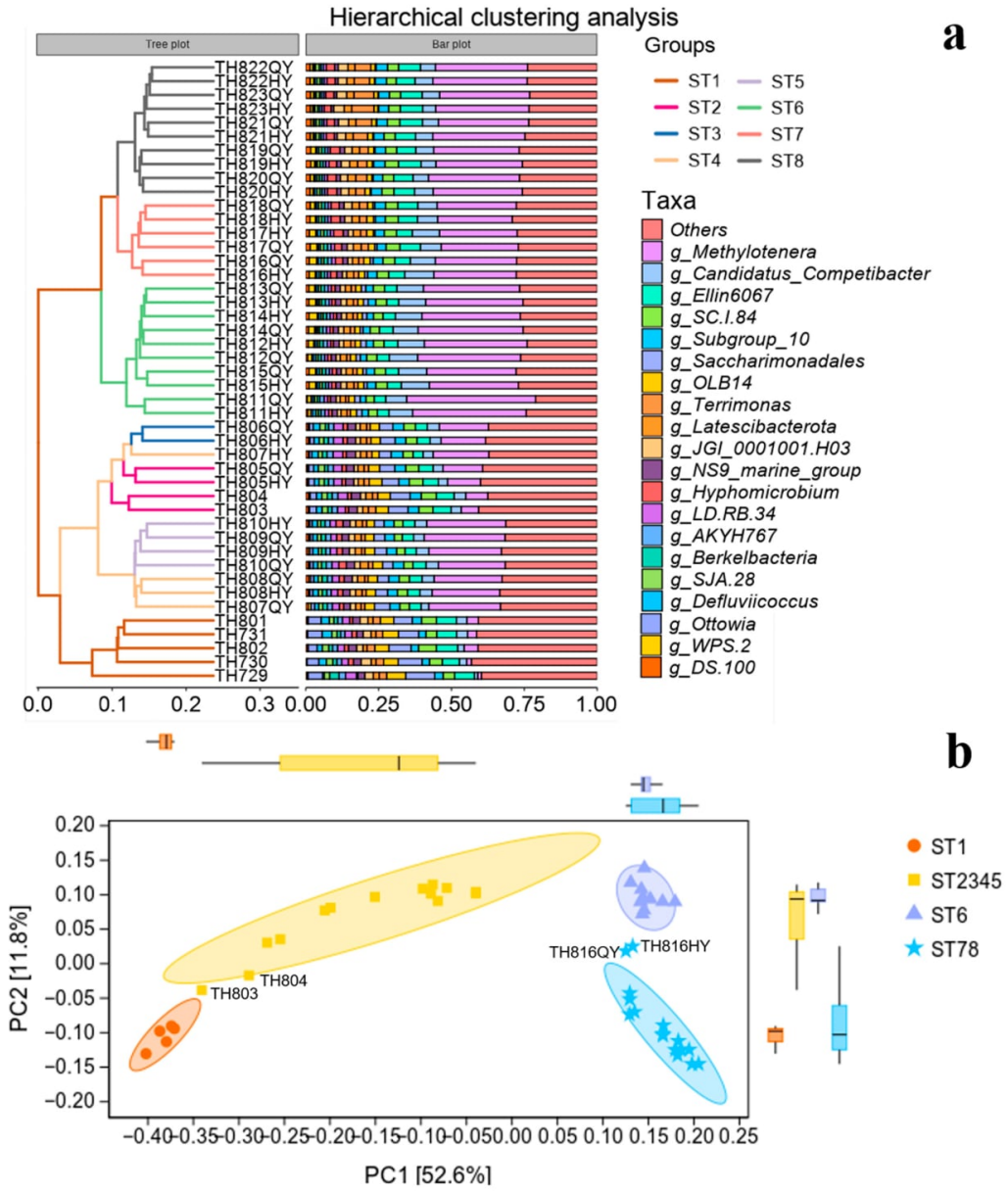


Figure 3. Hierarchical clustering analysis of microbial communities at the genus level among samples (**a**) and principal coordinate analysis (PCoA) at the Operational Taxonomic Unit (OTU) level based on all samples (**b**). Relative abundances in (**a**) were calculated excluding sequences unclassified at the genus level. "Others" comprises classified genera outside the top 20 in abundance.

To clearly show the stage-wise succession of the community, samples were divided into four major periods based on the clustering results: Stage 1, Stages 2–5, Stage 6, and Stages 7–8. PCoA was further performed at the OTU level based on the Bray–Curtis distance matrix (Figure 3b). The PCoA plot showed that the four periods were clearly separated along the first two principal coordinates. The first principal coordinate (PC1) explained 52.6% of the total variation, and the second principal coordinate (PC2) explained 11.8%. The marginal boxplots showed that Stages 1, 2–5, and 6 changed continuously from left to right along the PC1 axis and were significantly separated, while Stage 6 and Stages 7–8 were completely separated along the PC2 axis. The 95% confidence ellipses for the four periods were completely separated with no overlap, indicating significant differences in community structure among the stages ($p < 0.05$).

Based on the community composition and diversity results (Figures 2 and 3), the microbial community during the entire start-up process could be divided into four major

succession steps, which clearly correspond in time sequence to the eight process adjustment Stages. Step I was the environmental selection period, corresponding to Stage 1. After transfer from the wastewater treatment plant to the dredged residual water, the community underwent drastic reorganization, with a net loss of total biomass and *Methylotenera* accounting for less than 1% of the community. Step II was the function initiation and transition period, corresponding to Stages 2–5. Continuous influent and Carbon Source 1 dosing drove gradual biomass increase, and *Methylotenera* increased from below 1% to approximately 20%, although the brief switch to Carbon Source 2 temporarily stalled its growth. Step III was the disturbance response period (corresponding to Stage 6), where PAM dosing exerted strong selective pressure. The total biomass first rose and then fell sharply. At the same time, *Methylotenera* peaked at 34% and then declined to about 20%, indicating that PAM initially suppressed competing bacteria but later inhibited *Methylotenera* itself as toxicity accumulated. Step IV was the reconstruction period, corresponding to Stages 7–8. After PAM was stopped and PAC dosage was increased (Stage 7), and the No. 3 aeration tank was converted to anoxic (Stage 8), biomass increased with fluctuations but did not fully return to the pre-Stage 6 status. *Methylotenera* recovered to approximately 27% and remained the most abundant classified genus, reflecting its metabolic plasticity and ecological adaptability under oligotrophic and anoxic conditions. Throughout start-up, the aerobic and anoxic tanks showed highly similar community structures (Figures 2 and 3), mainly due to continuous mixing via the high sludge return ratio.

3.4. Changes in Microbial Functions

FAPROTAX functional prediction was performed based on 16S rRNA sequencing data to obtain the temporal variation characteristics of the community functional profile. Figure 4a shows the distribution of the top 10 functions in abundance, and Figure 4b shows the abundance changes in organic degradation functions (based on rarefied OTU data). The dominant functions, in descending order of proportion, were chemoheterotrophy, methylotrophy, methanol oxidation, nitrification/aerobic ammonia oxidation, aerobic chemoheterotrophy, fermentation, ureolysis, nitrogen fixation, nitrate reduction and hydrocarbon degradation.

For carbon degradation functions, chemoheterotrophy and methylotrophy (methanol oxidation) showed nearly identical abundance and trends: they increased steadily during Stages 1–3, decreased in Stage 4 after switching to Carbon Source 2, and slowly recovered in Stage 5 after switching back to Carbon Source 1. This result indicated that Carbon Source 1 was important for maintaining chemoheterotrophic and methylotrophic functions in the system. In Stage 6, both chemoheterotrophy and methylotrophy first increased and then decreased, consistent with trends in total biomass and *Methylotenera* abundance, indicating the negative influence of PAM dosing.

Regarding nitrogen transformation functions (Figure 4(c1,c2)), the abundance of nitrification/aerobic ammonia oxidation increased significantly in Stage 1, gradually decreased during Stages 2–4, briefly fluctuated in Stages 5 and 6 before recovering continuously from late Stage 6 onward to the end of Stage 8. Ureolysis and nitrogen fixation abundances were relatively low, generally increasing slightly and steadily during Stages 1–2, decreasing during Stages 3–5, decreasing further in Stage 6, and slowly recovering during Stages 7–8. Nitrate-reducing abundance was low but remained relatively stable during Stages 1–5 and continuously decreased during Stages 6–8.

FAPROTAX predictions indicated that the system tended toward enhanced methylotrophic metabolism during start-up, consistent with the continuous increase in the relative abundance of *Methylotenera*, suggesting that enrichment of this genus directly drove the increase in methylotrophic metabolic potential. For nitrogen transformation functions,

nitrification showed a decreasing trend in the middle period and recovered later, while nitrate reduction showed a continuous decrease. This contrasts with the system's efficient nitrogen removal performance, suggesting that it may not rely on the canonical complete nitrification–denitrification pathway for nitrogen removal, or that subpathways existed while FAPROTAX functional prediction cannot distinguish them.

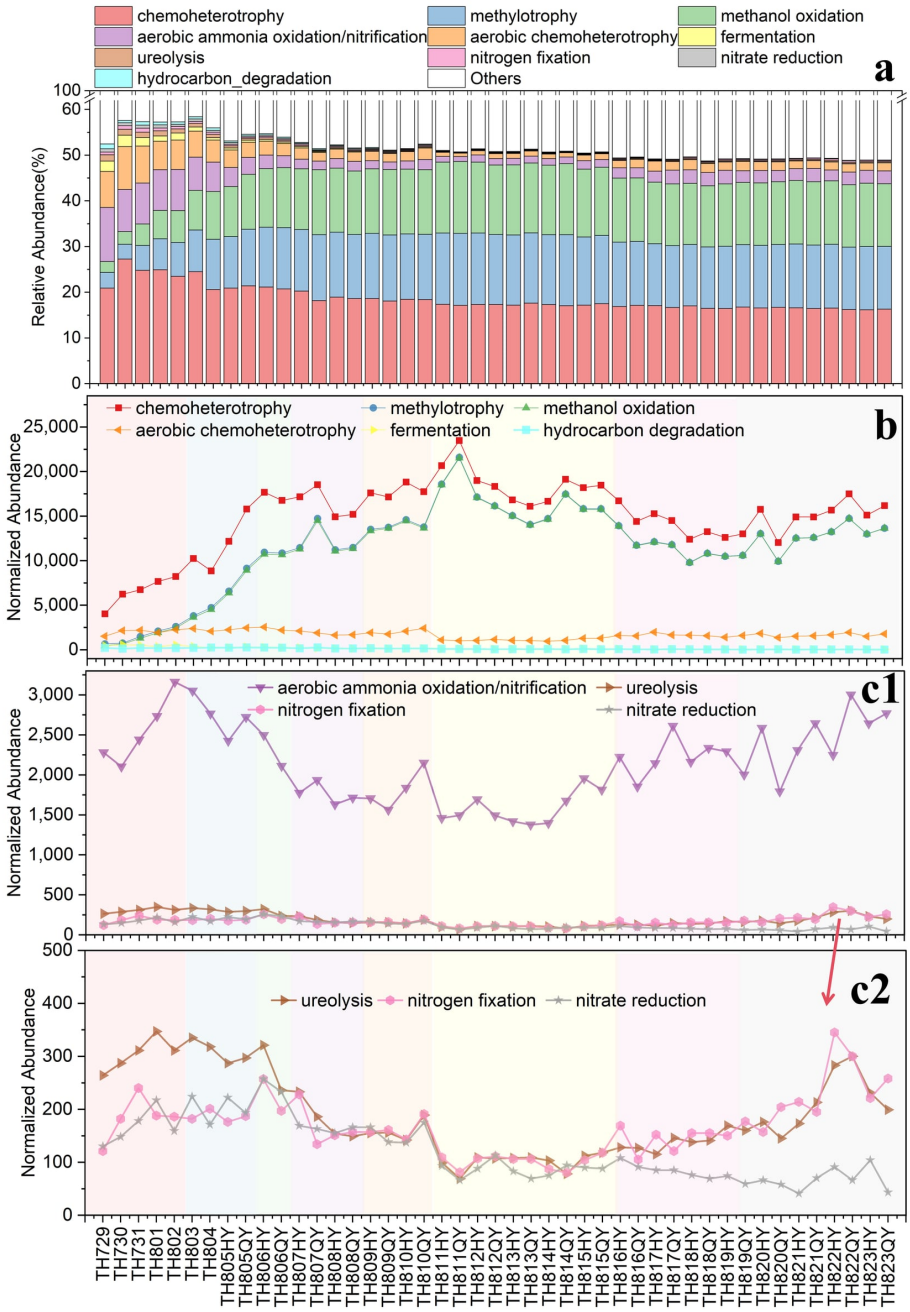


Figure 4. Changes in microbial functional abundance by Functional Annotation of Prokaryotic Taxa (FAPROTAX) functional prediction results (**a**) and abundance changes based on normalized OTU tables for organic degradation functions (**b**) and nitrogen transformation functions (**c1**,**c2**).

3.5. Changes in Microbial Physiological Activity

To evaluate the actual physiological response of microorganisms to process disturbances, four fluorescence staining methods were used to monitor the dynamic changes in respiratory activity, membrane integrity rate, metabolic activity, and DNA integrity rate. These four indicators reflect the physiological state of microorganisms in four ways:

energy metabolism (respiratory activity), structural integrity (membrane integrity rate), enzymatic function (metabolic activity), and genetic material (DNA integrity rate). The respiratory chain is located on the cell membrane and serves as the first line of defense in sensing external chemical stress; therefore, respiratory activity usually fluctuates early in the disturbance. A decrease in membrane integrity rate usually follows oxidative stress caused by respiratory chain damage. Metabolic activity usually decreases after membrane damage has accumulated to a certain extent. A decrease in DNA integrity rate requires more severe damage or prolonged continuous stress.

Figure 5a shows the trend of cellular respiratory activity detected by CTC/DAPI staining during process adjustment. In this experiment, data could not be collected during some stages because CTC is reduced by intracellular dehydrogenases to form water-insoluble formazan precipitates, and these hydrophobic precipitates can continue to grow inside bacterial cells until the cells burst [43] and can tightly aggregate cells through hydrophobic interactions, exacerbating cell agglomeration and making counting difficult. Based on the countable results, when Carbon Source 2 was switched back to Carbon Source 1 in Stage 5, the respiratory activity in the aerobic tank increased slightly from approximately 58% to 60%, while that in the anoxic tank decreased significantly from approximately 68% to 41%, indicating that carbon source type switching under anoxic conditions had a more pronounced effect on the respiratory chain. In Stage 6, respiratory activity in both the aerobic and anoxic tanks first increased significantly to approximately 80% and then decreased rapidly, and the aerobic tank was consistently higher than the anoxic tank, indicating that PAM inhibited the respiratory chain and that the anoxic environment amplified the inhibitory effect. After PAM dosing was stopped in the early Stage 7, respiratory activity recovered markedly. Fluorescence micrographs (Figure 5e–h) further confirmed fluctuations in respiratory activity. On 15 August (during PAM dosing in Stage 6), the red fluorescence signal in the anoxic tank was weak. In contrast, on 17 August (after PAM dosing was stopped in Stage 7), respiratory activity recovered significantly. In Stage 8, after converting the No. 3 aeration tank to an anoxic tank, respiratory activity continued to decrease to about 40% and recovered only slightly later. These results indicate that respiratory activity is highly sensitive to carbon source type and chemical dosing, and that anoxic conditions amplify its fluctuation amplitude.

Figure 5b shows the trend of microbial membrane integrity rate obtained by SYTO9/PI staining during process adjustment. In Stage 1, under static aeration, the membrane integrity rate increased slightly from 88% to above 90%, indicating that the inoculated sludge gradually adapted to the new environment. During Stages 2–6, the membrane integrity rate in both the aerobic and anoxic tanks remained above 85%, with little difference between the two, indicating that carbon source switching and PAM dosing had no obvious disturbance effect on membrane integrity rate. In Stage 7, the membrane integrity rate in both tanks decreased significantly, with a more pronounced change in the aerobic tank (decreasing to below 80%). We speculated that this phenomenon might arise from a delayed toxic effect of PAM. Although PAM dosing ceased in Stage 6, previously added PAM and its byproducts, particularly acrylamide monomers generated through anaerobic microbial or chemical degradation, may have continued to accumulate, causing cell membrane damage and DNA fragmentation [34,44]. However, the estimated average PAM exposure in Stage 6 was only ~0.15 mg/L. Even assuming industrial PAM products contain up to 0.1 wt% acrylamide (depending on national regulations), the theoretical average acrylamide concentration would not exceed 0.15 mg/L. Whereas acrylamide is generally considered toxic to microorganisms above 5 mg/L [45], despite a strict drinking water standard of 0.1 μg/L (EU) or 0.5 μg/L (WHO). Thus, acute acrylamide toxicity was unlikely to be the primary driver of the microbial suppression. Instead, these decreases also coincided with

the increased PAC dosage in Stage 7 (average net dosage as high as 58.3 mg/L). PAC may hydrolyze in the environment to release Al^{3+}, which not only causes oxidative stress and enzyme inactivation [46] but also results in pH decrease (Figure S2c), further contributing to cellular membrane stress. By Stage 8, membrane integrity in both tanks recovered somewhat, fluctuating around 85%, but remained lower than before Stage 7.

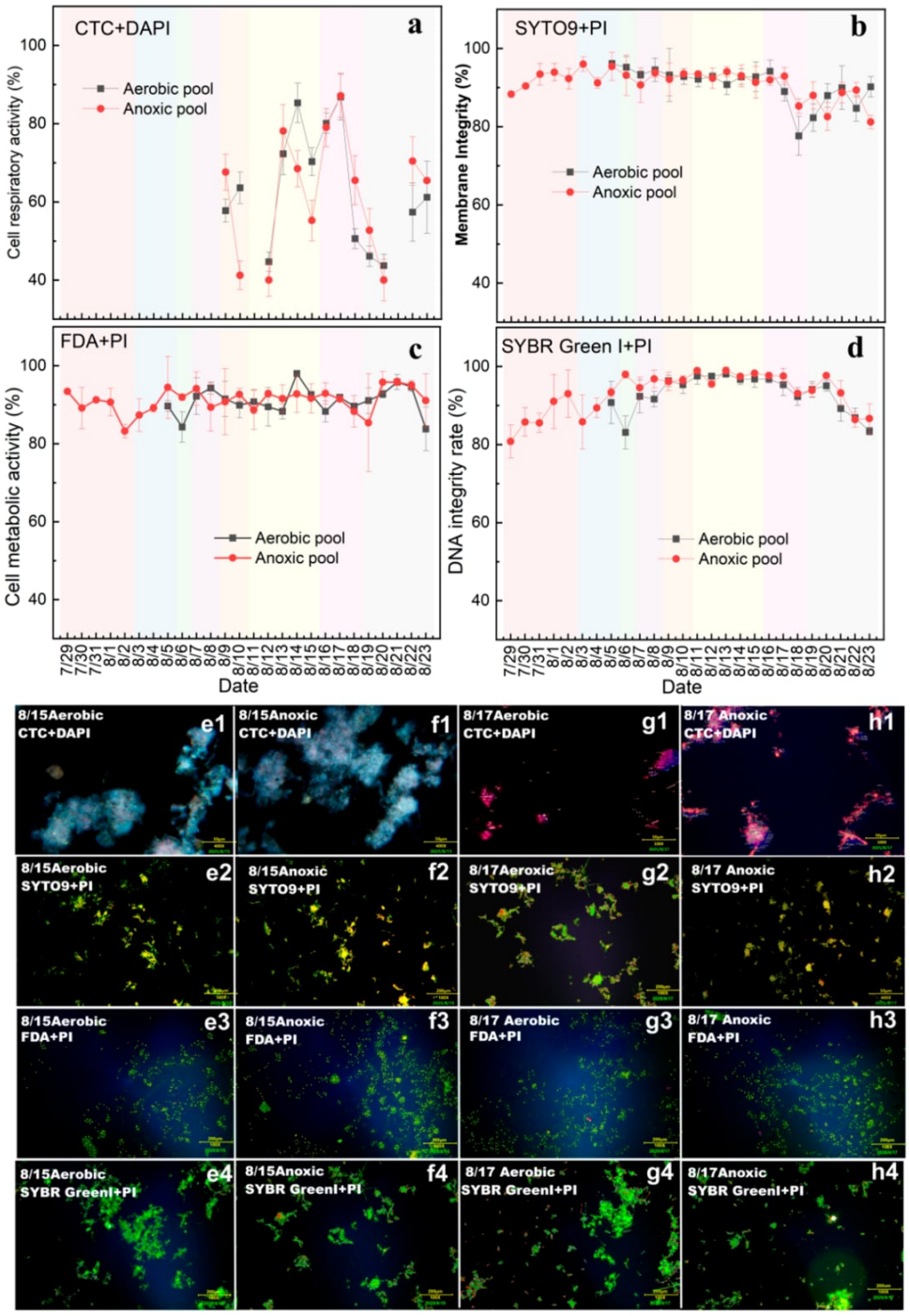


Figure 5. Microbial physiological activity evolution during start-up: respiratory activity (**a**) and corresponding fluorescent micrographs (**e1**–**h1**); membrane integrity rate (**b**) and corresponding micrographs (**e2**–**h2**); metabolic activity (**c**) and corresponding micrographs (**e3**–**h3**); DNA integrity rate (**d**) and corresponding micrographs (**e4**–**h4**). (**e**,**f**) represent samples from the aerobic and anoxic tanks on 15 August and (**g**,**h**) represent samples from the aerobic and anoxic tanks on 17 August, respectively. Scale bars: 200 μm for rows 1–3 and 50 μm for row 4.

Figure 5c shows the trend of cellular metabolic activity detected by FDA/PI double staining during process adjustment. During ambient-temperature start-up, metabolic activity was generally high (above 80%). In the static aeration stage, metabolic activity decreased from 93% to 83%, indicating that microorganisms were adapting and adjusting. In Stage 2, with carbon source dosing, cellular metabolic activity recovered significantly to above 90%. In Stage 3, metabolic activity in the anoxic tank remained above 90%, while that in the aerobic tank decreased to below 85% and then recovered, which may be related to the oxidative stress response caused by PAC dosing mentioned above. During Stages 4–7, metabolic activity in both the aerobic and anoxic tanks mostly fluctuated around 90%, with only a slight decrease in the anoxic tank at the end of Stage 7, consistent with the preceding decrease in membrane integrity rate, indicating that the delayed effect of PAM or the increased PAC dosage also had some effect on metabolic activity. In Stage 8, metabolic activity first increased and then continuously decreased, indicating that anoxic conditions generally inhibit cellular metabolic activity.

Figure 5d shows that the DNA integrity rate detected by SYBR Green I/PI double staining remained above 80% overall. In Stage 1, it increased from 80% to above 90%, synchronized with the improvement in membrane integrity rate. In Stage 2, it briefly decreased, then recovered. In Stage 3, the DNA integrity rate in the aerobic tank briefly decreased to 80%, and the membrane integrity rate and metabolic activity also decreased synchronously, confirming that PAC dosing and Al^{3+} generated by hydrolysis may damage microbial activity by causing oxidative stress and enzyme inactivation [46]. During Stages 4–6, the DNA integrity rate remained above 90%, indicating that carbon source switching and PAM dosing had limited effects. In late Stage 7, it also decreased slightly, similar to the changes in respiratory activity, membrane integrity rate, and metabolic activity. After the anoxic conversion in Stage 8, the DNA integrity rate in both tanks briefly recovered and then rapidly decreased to approximately 80%, similar to the trend of metabolic activity, indicating that anoxic conditions are generally unfavorable for DNA repair.

3.6. Influence of Environmental Factors on Microbial Community

To investigate the driving effects of environmental factors on the microbial community structure, redundancy analysis (RDA) was performed on the genus-level microbial community abundance data (Hellinger-transformed) using chemical dosage (Carbon Source 1, Carbon Source 2, PAC, and PAM) and influent water quality indicators (COD, NH_4^+-N, TN and pH) as explanatory variables. The results are shown in Figure 6a. Since Stage 1 had not yet started continuous influent monitoring and no relevant indicator records were available, it was not included in the correlation analysis. The permutation test indicated that the overall model was significant ($p = 0.001$), and the first two axes cumulatively explained 62.19% of the total variation (RDA1: 48.33%, RDA2: 13.86%). Samples separated clearly in ordination space into three periods: Stages 2–5, Stage 6, and Stages 7–8. Stages 2–5 separated from the other two groups along the RDA1 axis, while samples from Stage 6 and Stages 7–8 separated clearly along the RDA2 gradient, consistent with the four-step succession pattern revealed by PCoA analysis (Figure 3b), indicating that the selected environmental factors had strong overall explanatory power for the whole community structure.

Marginal effect tests further quantified each environmental factor's independent contribution. PAM dosing had the highest contribution ($r^2 = 0.685$, $p < 0.001$), with a loading of 0.997 on the RDA2 axis, indicating that PAM dosing was the dominant factor driving the specific separation of Stage 6 samples from those of other stages along the RDA2 axis. Carbon Source 2 dosage ($r^2 = 0.252$, $p = 0.005$) and influent TN ($r^2 = 0.199$, $p = 0.021$) contributed secondary variation in the ordination space, among which Carbon Source 2 had a loading of −0.966 on the RDA1 axis, dominating the distribution of Stages 2–5

samples in the negative half of RDA1. This result was highly consistent with the temporal trajectory of community succession: after the brief switch to Carbon Source 2 in Stage 4, the increase in *Methylotenera* abundance stalled (Figure 2c), and effluent TN increased transiently (Figure 1a), indicating that pure acetate as a single carbon source could not effectively maintain the metabolic activity and nitrogen removal function of methylotrophic bacteria. Influent TN had a loading of −0.854 on the RDA2 axis, corresponding to the distribution characteristics of Stages 7–8 samples in the negative half of RDA2. PAC dosage ($r^2 = 0.178$, $p = 0.035$) had a loading of 0.887 on the RDA1 axis, opposite that of Carbon Source 2, reflecting the divergent effects of chemical flocculant and carbon-source switching on community structure. In contrast, the marginal effects of Carbon Source 1 dosage ($r^2 = 0.023$, $p = 0.668$), influent COD ($r^2 = 0.003$, $p = 0.955$), and influent NH_4^+-N ($r^2 = 0.101$, $p = 0.159$) did not reach significant levels, indicating limited independent explanatory power for community structure variation. Overall, PAM dosing, Carbon Source 2 dosing, influent TN, and PAC dosing had relatively large effects on the microbial community structure.

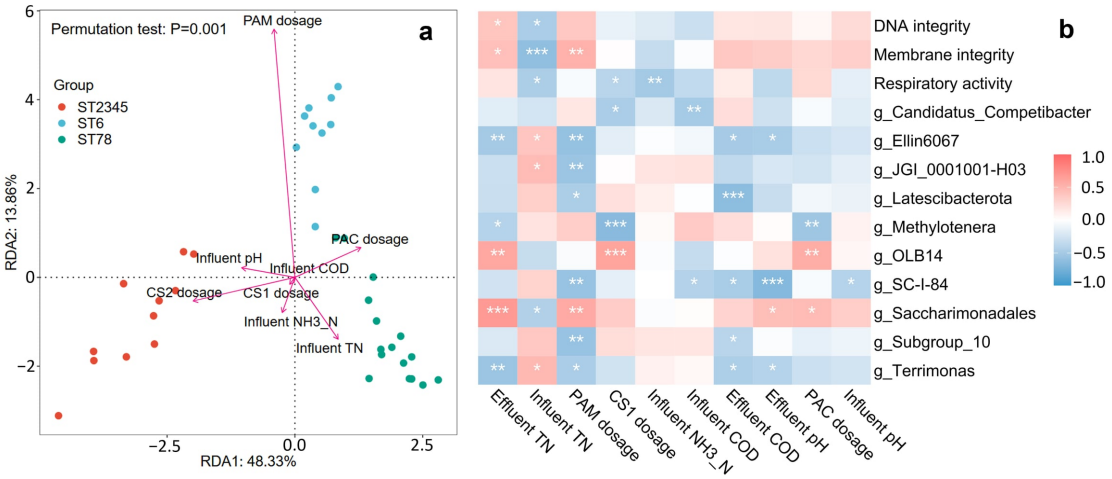


Figure 6. Redundancy analysis (RDA) results between microbial community structure (genus level) and environmental factors (influent indicators and chemical dosage) (**a**); Spearman correlation heatmap of most abundant classified genera and microbial activity with key environmental factors (**b**). Red and blue represent positive and negative correlations, respectively, and the color intensity indicates the magnitude of the correlation coefficient (r). * $p < 0.05$, ** $p < 0.01$, *** $p < 0.001$.

To further elucidate the possible executors during community succession and their sensitivity to process and water quality, Spearman correlation analysis was performed between the abundance of the top 10 most abundant genera and microbial activity indicators and influent/effluent water quality and chemical dosage. Figure 6b shows that, for nitrogen-related water quality indicators, effluent TN was significantly negatively correlated with the abundance of *g-Methylotenera*, *g-Ellin6067*, and *g-Terrimonas*, suggesting that these three genera may be involved in efficient nitrogen removal in the system. According to previous reports, the most abundant genus, *Methylotenera*, in this study has a complete denitrification pathway. It uses one-carbon compounds (such as methanol) as carbon sources and electron donors, and can perform denitrification even under aerobic or microaerobic conditions [37,47]. *Ellin6067* is an ammonia-oxidizing bacterium widely distributed in nature and wastewater treatment systems, participating in the first half of nitrification and providing sufficient substrate for denitrification, rather than directly participating in the final removal of TN [40]. *Terrimonas* belongs to the phylum *Bacteroidetes*, and some species have been reported to possess aerobic denitrification ability [48]. Therefore, it is speculated that the three form a functionally complementary cooperative network of substrate

supply (*Ellin6067*), aerobic denitrification (*Terrimonas*), and methylotrophic denitrification (*Methylotenera*), jointly driving efficient nitrogen removal in the system. Among them, the relative abundance of *Methylotenera* increased explosively from less than 1% initially to 34% (Figure 2b), much higher than that of *Ellin6067* and *Terrimonas*, indicating that this genus may play an important role in the denitrification functional network. In addition, two other genera in the system may also participate in nitrogen transformation. For example, *Candidatus Competibacter*, a typical glycogen-accumulating organism (GAO), can drive endogenous denitrification under anoxic conditions using glycogen stored under aerobic conditions [38]. Similarly, *SC-I-84* has been identified as a novel partial denitrifying bacterium [39]. However, both pathways are incomplete and limited to reducing nitrate to nitrite, lacking the ability to reduce nitrite to nitrogen further.

The abundances of *g-Ellin6067* and *g-Terrimonas* were positively correlated with influent TN, whereas the positive correlation between *g-Methylotenera* and influent TN was not significant. This result indicates that nitrogen-containing substrates directly drive the proliferation of *Ellin6067* and *Terrimonas*, whereas multiple factors may influence the proliferation of *Methylotenera*. Influent and effluent NH_4^+-N showed no significant correlation with the abundance of any genus.

Regarding chemical dosing, PAM dosage was negatively correlated with the abundances of multiple genera, including *g-Ellin6067, g-JGI0001001-H03, g-Latescibacterota, g-SC-I-84, g-Subgroup_10, and g-Terrimonas,* indicating that PAM exerted broad-spectrum inhibition on the community, with only a few tolerant genera (e.g., *Saccharimonadales*) persisting. Notably, Carbon Source 1 dosage was negatively correlated with *Methylotenera* abundance. Because the main carbon source was continuously dosed throughout the process, it should theoretically have provided substrate support for *Methylotenera*. However, a negative correlation between them was observed statistically. Combined with the temporal data, this phenomenon more likely reflects a temporal mismatch between abundance and dosage. When *Methylotenera* abundance peaked at 34% in Stage 6, the dosage of Carbon Source 1 was not the highest. In contrast, in Stage 7, when its abundance declined to 22%, the dosage of Carbon Source 1 was relatively high (Figure S1a). Meanwhile, the proliferation of *Methylotenera* may be regulated by multiple factors (e.g., PAM and PAC dosing) or exhibit a lag effect in response to carbon sources, rather than following a simple linear relationship. Among these, PAC dosage was significantly negatively correlated with *g-Methylotenera*, indicating that its chemical stress may have a certain inhibitory effect on the proliferation of this most abundant genus, possibly due to oxidative stress damage induced by Al^{3+}, as mentioned above [46].

Regarding physiological indicators, respiratory activity, membrane integrity rate, and DNA integrity rate were all negatively correlated with influent TN, and membrane integrity rate and DNA integrity rate were also positively correlated with effluent TN. This result may mainly reflect temporal co-variation. Influent TN was at a stage-specific high level during the late start-up period (Stages 7–8), while respiratory activity, membrane integrity rate, and DNA integrity rate simultaneously declined during this period due to the cumulative effect of PAM and anoxic conversion. This temporal overlap may have produced negative correlations. Effluent TN showed two high-value periods in Stage 4 (carbon source switching) and Stages 7–8 (delayed effect of PAM), and its overall trend was statistically synchronized with the decline in membrane integrity rate and DNA integrity rate from high to low levels. In addition, respiratory activity was negatively correlated with influent NH_4^+-N. On the one hand, this may also reflect temporal co-variation. On the other hand, free ammonia (FA, NH_3) has been reported to directly act on respiratory chain complexes in the cell membrane and interfere with electron transport efficiency [49]. Combined with the characteristic that respiratory activity fluctuated more significantly under anoxic conditions

(Figure 5a), it is speculated that under anoxic conditions, nitrification is inhibited and the increase in free ammonia concentration may exert a certain direct inhibitory effect on the respiratory chain.

3.7. Mechanisms of Nitrogen Removal During Platform Start-Up

In biochemical water treatment processes, external carbon sources are usually required to enhance nitrogen removal performance when influent exhibits a typical low C/N ratio [50]. In this study, continuous dosing of Carbon Source 1 composite carbon source (acetate, methanol and ethanol) supported relatively good nitrogen removal. Correlation analysis indicated that *Methylotenera*, the most abundant classified genus, was probably a key genus driving nitrogen removal in the system, and continuous supply of Carbon Source 1 was crucial for its function. To resolve the nitrogen removal mechanism at the molecular level, representative samples were selected from the initial start-up (29 July), middle (10 August, aerobic and anoxic tanks, Stage 5), and late (21 August, aerobic and anoxic tanks, Stage 8) periods for metagenomic sequencing. Carbon and nitrogen metabolic pathways were annotated using the DiTing tool and jointly analyzed with KEGG functional gene abundances. It should be noted that gene upregulation or downregulation does not correspond strictly to functional expression and the gene-level results below are therefore used to infer pathway-level trends rather than to quantify the contribution of each pathway.

Carbon metabolic pathway abundances annotated by DiTing (Figure 7a) showed that the most abundant pathways were glycolysis (glucose into pyruvate), TCA cycle (acetyl-CoA into CO_2), and the acetate conversion module (acetate into acetaldehyde and then into ethanol). In addition, the acetyl-CoA-to-acetate conversion pathway also showed moderate abundance. Comparison among samples from different periods revealed that the pathways with significantly increased abundance in the middle and late periods were mainly methanol oxidation to formaldehyde and formate oxidation to CO_2. In addition, lactate-to-acetate conversion and the autotrophic carbon fixation pathways CBB, 3HB, and WL were also upregulated. In contrast, the methane metabolism pathway decreased significantly in the middle and late periods, and the reductive TCA (rTCA) autotrophic carbon fixation pathway and pyruvate fermentation to acetate/formate pathway were also downregulated. The functional gene abundance heatmap in Figure 7b further confirmed the activation of these pathways at the molecular level. At the C1 carbon source utilization level, the methanol oxidation gene *mxaF* was significantly upregulated in the middle period and declined later. Formaldehyde metabolism genes *fae*, *frmA*, *fdhA* (K00148), and *hps-phi* were upregulated to varying degrees in the middle and late periods, and key genes for formate metabolism, *fdhF*, *fdhA* (K05299), and *fhlA*, were also significantly upregulated in the middle and late periods. At the C2 carbon source utilization level, the acetate activation gene *acs* (acetate into acetyl-CoA) was significantly enriched in the middle and late periods, and ethanol oxidation genes *adh*/*ald* were coordinately upregulated, indicating that acetate and ethanol utilization pathways were simultaneously activated. Meanwhile, key genes *pta*/*ackA* for the hydrolysis of acetyl-CoA to replenish acetate were also upregulated to varying degrees in the middle and late periods, forming a bidirectional acetate/acetyl-CoA conversion loop with *acs*. At the central carbon metabolism level, glycolysis genes (*glk*/*pfkA*/*pyk*) were upregulated to varying degrees in the middle and late periods. At the central carbon metabolism junction, *pdhA* (pyruvate into acetyl-CoA) and the TCA cycle entry gene *gltA* were upregulated to varying degrees in the middle and late periods, whereas *pflA* (pyruvate into formate and acetyl-CoA) showed a downward trend.

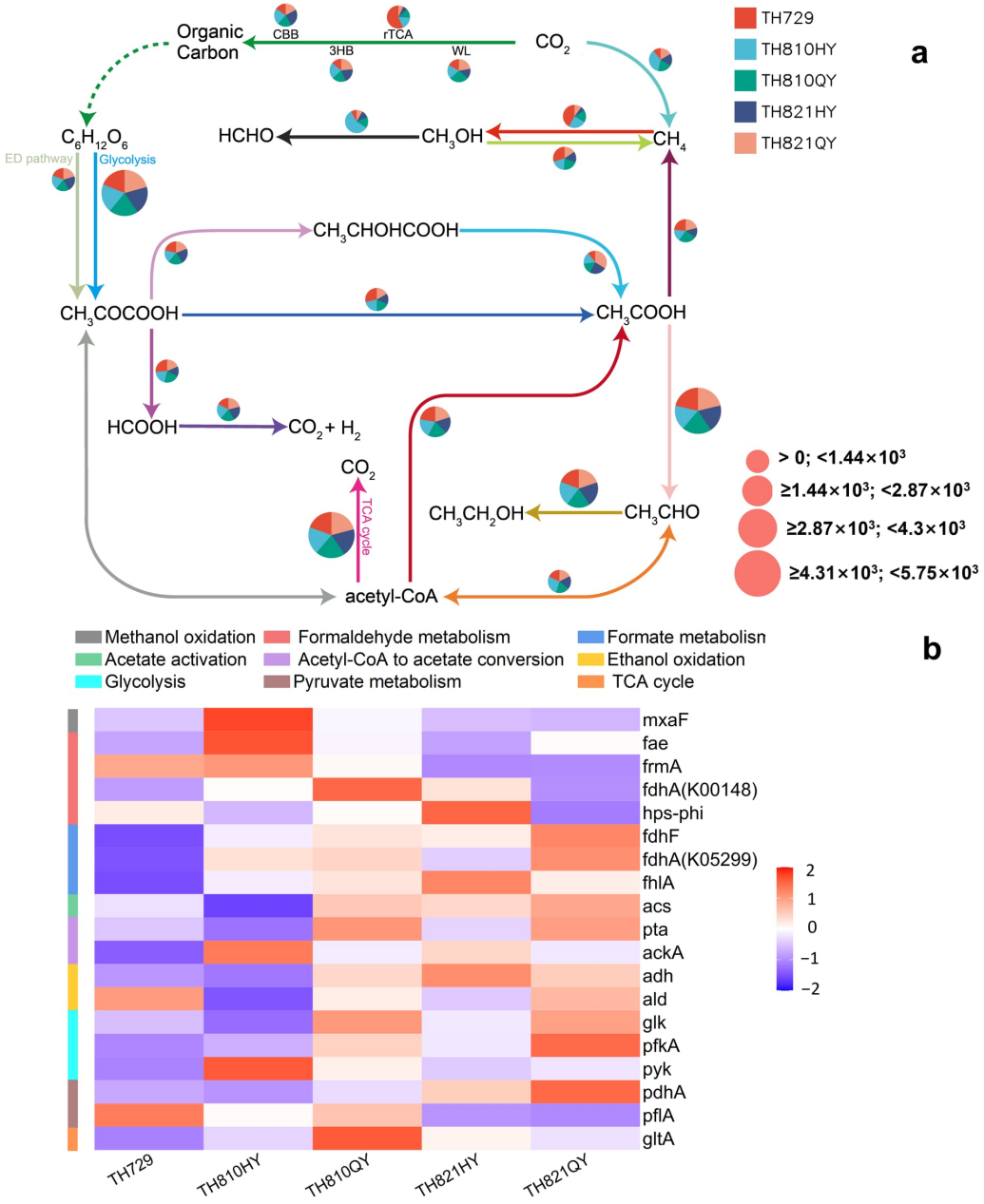


Figure 7. Changes in the abundance of metagenomic carbon metabolic pathways annotated by the DiTing tool (**a**) and related functional gene abundance annotated by Kyoto Encyclopedia of Genes and Genomes (KEGG) (**b**). In the pathway diagram, bubble size represents pathway abundance (expressed as normalized Transcripts Per Million (TPM)), and the fan-shaped sectors represent the proportion of each sample's pathway abundance relative to the total across all samples. In the heatmap, gene abundance (rows) was Z-score standardized and color represents relative abundance across samples.

Nitrogen metabolic pathway abundances based on DiTing annotation (Figure 8a) showed that the most active pathways were concentrated in denitrification (nitrate reduction, nitrite reduction and N_2O reduction) and downstream of nitrification (nitrite oxidation to nitrate). In addition, dissimilatory nitrate reduction to ammonium (DNRA) and assimilatory nitrate reduction to ammonium (ANRA) pathways also exhibited relatively high abundances. However, the anammox pathway was not detected. Comparison among samples from different periods revealed that the pathway abundances of nitrogen fixation and ANRA increased markedly during the middle and late start-up periods, whereas the

abundance of the first part of nitrification (ammonia oxidation) decreased significantly. The gene abundance heatmap (Figure 8b) further confirmed these trends at the molecular level. The abundance of the nitrogen fixation gene *nifH* increased in the middle and late periods. The abundances of the nitrification genes *amoA* and *hao* generally showed a downward trend compared with the initial stage, whereas *nxrA* (nitrite oxidation to nitrate) first decreased and then increased. Among denitrification genes, the key genes for nitrate reduction to nitrite, *narG* and *napA*, increased to varying degrees compared with the initial stage. Regarding nitrite reduction to NO, there are two key genes, *nirK*- and *nirS*-type enzymes sharing similar functions, which rarely appear in the same genome, although each can compensate for the absence of the other [51]. During the start-up, *nirK* was downregulated in the middle and late periods, whereas *nirS* was upregulated. The gene for NO reduction to N_2O, *norB*, fluctuated downward, while the gene for N_2O reduction to N_2, *nosZ*, first increased and then decreased. The DNRA genes *nrfA* and *nirB/D* generally showed a fluctuating downward trend compared with the initial stage. The ANRA genes *nasA* and *nirA* were upregulated to varying degrees in the middle and late periods. The abundance changes in genes related to organic nitrogen metabolism were further analyzed. The ammonia assimilation genes *gdhA* (glutamate dehydrogenase), *glnA* (glutamine synthetase), and *gltB/gltD* (glutamate synthase) increased to varying degrees during the middle and late start-up periods. Regarding organic nitrogen mineralization, the urea decomposition gene *ureC* also showed a significant upward trend during the middle and late start-up periods.

Comparison of the metagenomic and FAPROTAX results showed general consistency in the qualitative trends of functional succession. For carbon metabolism, both indicated enhanced methylotrophy/methanol oxidation in the middle period and a later decline. For nitrogen metabolism, both indicated an overall decline in nitrification and increases in nitrogen fixation and urea hydrolysis in the middle and late periods. However, the two approaches differed in pathway resolution. FAPROTAX indicated a continuous decline in the aggregated nitrate reduction function during Stages 6–8, whereas metagenomics revealed upregulation of the nitrate reduction genes (*narG*/*napA*), a downregulation in *nirK*, and an upregulation of *nirS*. The two are not contradictory but reflect different observational levels due to their distinct inference principles. FAPROTAX maps 16S taxa to literature-curated process-level functions and reports only an aggregated denitrification/nitrate-reduction potential, without resolving gene carriage or *nirK*/*nirS* host identity. This methodological limitation is not unique to FAPROTAX. Phylogenetic investigation of communities by reconstruction of unobserved state (PICRUSt) based prediction of activated sludge functions has also been reported to rarely annotate ammonia oxidation genes (*amo*), even in systems where nitrification is known to occur. In contrast, metagenomics directly quantifies individual genes and distinguishes the two nitrite reductase isoenzymes.

Based on the metagenomic data shown in Figures 7 and 8, the coupled carbon and nitrogen metabolic pathways in the late start-up period (represented by the anoxic tank sample on 21 August) are summarized in Scheme 2. Within the central carbon metabolism module, acetate and ethanol from the composite carbon source entered central metabolism through multiple pathways. Acetate was activated to acetyl-CoA by *acs* and then entered the TCA cycle. Ethanol was oxidized by *adh/ald* to acetate and then to acetyl-CoA, entering the TCA cycle. Methanol was oxidized to formaldehyde by *mxaF* and participated in C1 metabolism. These genes were upregulated to varying degrees during the middle and late start-up periods (Figure 7b), indicating that the uptake and activation of each carbon source substrate were fully activated. In addition, glycolysis-related genes (*glk*/*pfkA*/*pyk*) were also upregulated to varying degrees during the middle and late start-up periods (Figure 7b). Given the absence of glucose in the external carbon feed, the substrate for glycolysis should originate from endogenous glycogen. In this system, glycogen-accumulating organisms

such as *Candidatus Competibacter* synthesize glycogen under aerobic conditions and degrade it to pyruvate under anoxic conditions to fuel glycolysis [52]. Pyruvate could be converted to acetyl-CoA by *pdhA* and enter the TCA cycle or alternatively fermented into formate by *pflA*. The significant upregulation of *pdhA* and concurrent downregulation of *pflA* during the middle and late start-up stage (Figure 7b) indicated that carbon flux was preferentially directed toward complete oxidation via the TCA cycle rather than fermentation. C1 compound metabolism proceeded via multiple parallel pathways. Methanol in the carbon source was oxidized to formaldehyde by *mxaF*. Formaldehyde could be converted to formate via the H_4MPT-dependent pathway (*fae*) or via the glutathione-dependent pathway (*frmA*) or via the glutathione-independent pathway (*fdhA*). Formaldehyde may additionally be assimilated directly into central carbon metabolism for biomass synthesis via the RuMP assimilation pathway (*hps-phi*). The upregulation of *fae* and downregulation of *fdhA* and *hps-phi* indicated that formate production via the H_4MPT-dependent pathway was the main route for formaldehyde oxidation in the system. This pathway is widely distributed among proteobacterial methylotrophs [53], and certain methylotrophs rely exclusively on it to oxidize formaldehyde generated from methylamine catabolism [54]. As a central hub of C1 metabolism, formate was oxidized to CO_2 through three parallel pathways: (1) NAD^+-dependent formate dehydrogenase (*fdhF*) yielding NADH; (2) $NADP^+$-dependent formate dehydrogenase (*fdhA*, K05299) generating NADPH; and (3) the formate hydrogenlyase complex (*fhlA*) splitting formate into CO_2 and H_2, serving as a relief mechanism against anoxic formate accumulation. Metagenomic results (Figure 7b) showed coordinated upregulation of these three pathways during the middle and late start-up periods, establishing a sustained supply of NADH and NADPH for downstream nitrogen metabolism, as well as a hydrogen-releasing safety valve to mitigate formate accumulation under anoxic conditions.

Carbon and nitrogen metabolism were coupled through two mechanisms. The first was energy coupling: NADH generated from pyruvate oxidative decarboxylation, C1 compound oxidation and the TCA cycle supplied electron donors for the denitrification chain [37,47]. The C1 oxidation pathway provided an additional NADPH supply channel through formate oxidation (via *fdhA*), which could support the ammonia assimilation pathway. Second, carbon skeleton coupling: α-ketoglutarate, a TCA cycle intermediate, could provide carbon skeletons for the ammonia assimilation pathway in nitrogen metabolism. The increased consumption of α-ketoglutarate by assimilation pulled enhanced carbon flux into the TCA cycle, shifting carbon skeletons from oxidative energy production toward metabolite output.

Within this framework, Scheme 2 further illustrates nitrogen metabolism. Ammonia sources in the system included influent NH_4^+, biological nitrogen fixation, organic nitrogen hydrolysis (e.g., urea decomposition), and nitrate reduction via the ANRA pathway. Metagenomic data revealed that the upstream nitrification pathway (ammonia oxidation and hydroxylamine oxidation to nitrite) exhibited low overall abundance, whereas the downstream nitrite-oxidizing module (nitrite oxidation to nitrate) was relatively abundant (Figure 8a). Meanwhile, significant upregulation of the key genes for nitrogen fixation (*nifH*), urea decomposition (*ureC*) and the upstream ANRA gene (*nasA*) during the middle and late start-up periods (Figure 8b) indicated that the system actively supplemented ammonia nitrogen through multiple pathways to counteract nutrient limitation imposed by low influent NH_4^+-N concentrations. Both the high-affinity GS-GOGAT pathway (*glnA*/*gltB*/*gltD*) and the low-affinity GDH pathway (*gdhA*) were upregulated, reflecting active ammonia assimilation with α-ketoglutarate to form glutamate. In contrast, the key genes of front-end nitrification, the ammonia oxidation process (*amoA* and *hao*), were downregulated and exhibited an order-of-magnitude lower abundance. Alternative non-canonical ammonia oxidation pathways, including key genes of the dirammox pathway (*dnf*), the pyruvic oxime dioxygenase pathway (*pod*), and the anammox pathway (hzs, hdh), were not detected. Col-

lectively, these findings demonstrate activated ammonia assimilation alongside suppressed ammonia oxidation compared to the initial sludge.

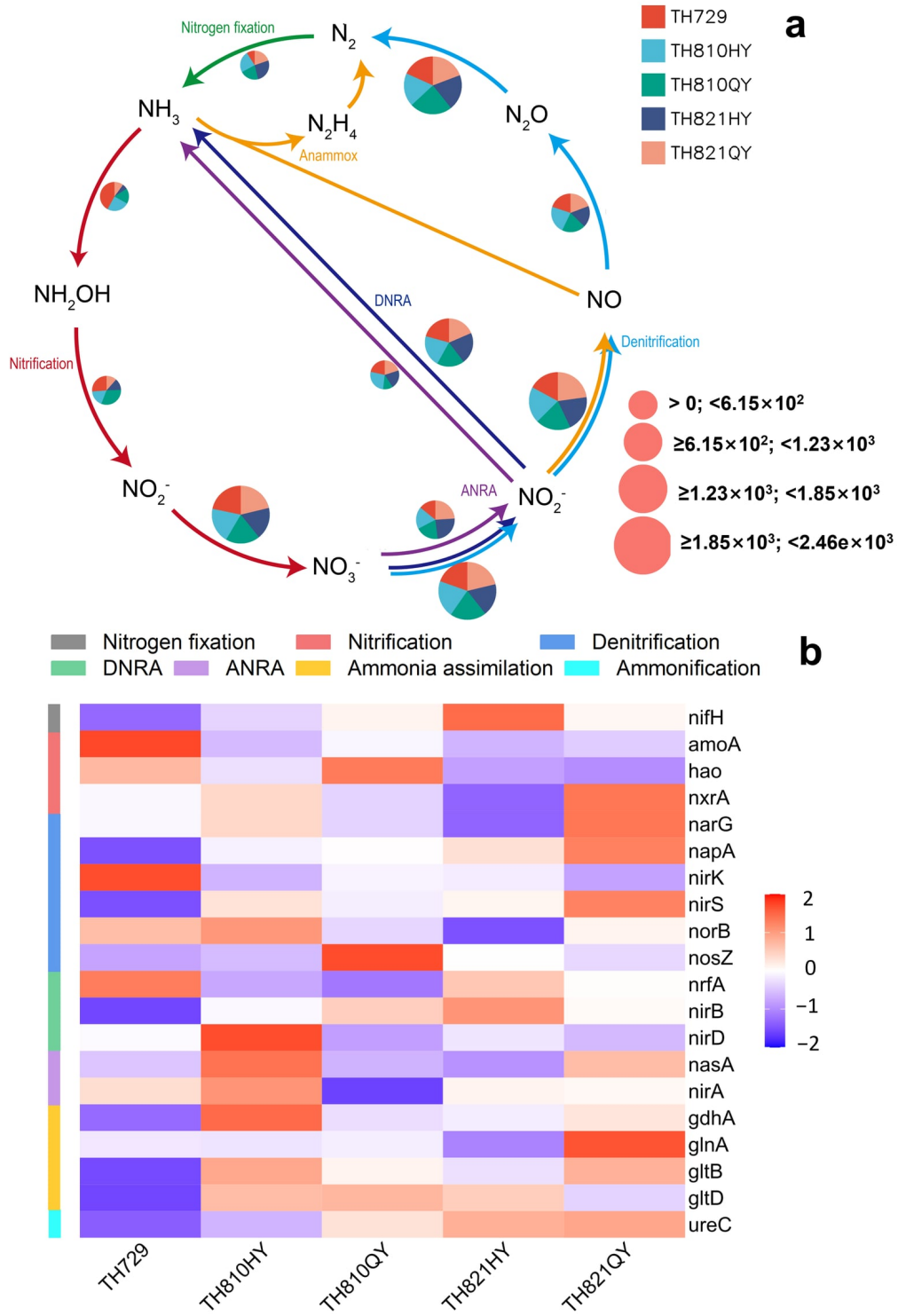
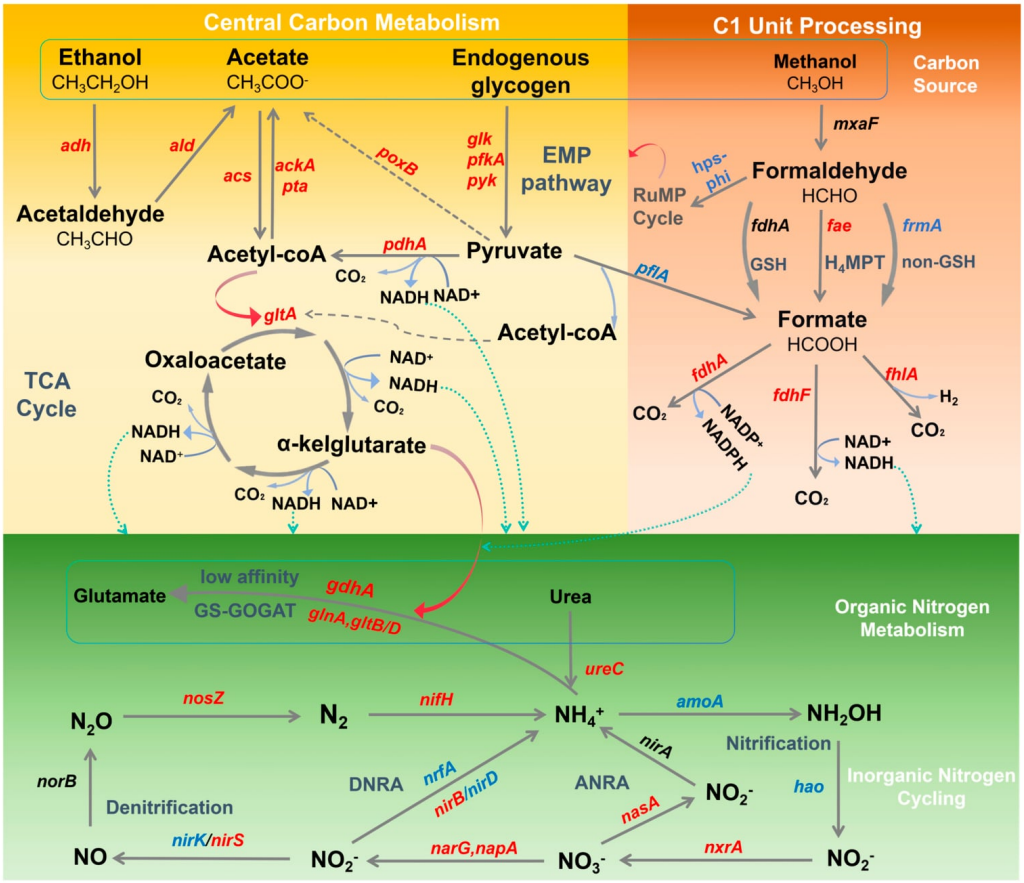


Figure 8. Changes in the abundance of metagenomic nitrogen metabolic pathways annotated by the DiTing tool (**a**) and related functional gene abundance annotated by KEGG (**b**). In the pathway diagram, bubble size represents pathway abundance (normalized TPM), and the fan-shaped sectors represent the proportion of each sample's pathway abundance relative to the total across all samples. In the heatmap, gene abundance (rows) was Z-score standardized, and color represents relative abundance across samples.



Scheme 2. Schematic diagram of the coupled carbon and nitrogen cycling metabolic pathways of the microbial system in the residual water treatment platform.

The repression of ammonia oxidation genes (*amoA*, *hao*), together with the decline of the ammonia-oxidizing bacterium *Ellin6067* (Figure 2c), probably arose from competitive selection under the applied influent and mixed carbon-source conditions. At the low influent NH_4^+-N in the present work (average 3.78 mg/L), ammonia-oxidizing bacteria (AOB) suffered substrate scarcity and became less competitive than other species [55,56]. Previous studies have shown that acetate addition can reduce AOB populations and disrupt nitrification in biofilm reactors [57], and further confirmed that acetate input lowers AOB and *amoA* diversity in activated sludge [55]. Methanol, by contrast, stimulates methylotrophic growth while inhibiting AOB and *amo* enzyme activity [58]. Accordingly, the enrichment of *Methylotenera* with Carbon Source 1 (acetate, methanol and ethanol) intensified this competitive pressure, restraining AOB and ammonia oxidation while enabling methylotrophic denitrification to prevail. However, it should also be noted that transcript and protein expression cannot be directly inferred from gene abundance alone. Nitrification was downregulated but not necessarily eliminated and less abundant but active AOB such as *Ellin6067* may still participate in NH_4^+-N oxidation for subsequent nitrite oxidation (which was upregulated).

Nitrate fate included denitrification, DNRA and ANRA pathways. Metagenomic results showed that denitrification possessed the highest overall gene abundance, followed by DNRA, whereas ANRA was relatively lower in abundance. During the middle and late start-up periods, denitrification genes *narG*, *napA*, *nirS* and *nosZ* were upregulated to varying degrees. In contrast, *nirK* and *norB* were downregulated. As mentioned above, *nirS* and *nirK* encode functionally redundant nitrite reductases that can compensate for one another. The downregulation of *nirK* and upregulation of *nirS* revealed an isoenzyme-level niche restructuring during start-up. In the initial active sludge, *nirS* was moderately more

abundant than *nirK* (approximately 1.2-fold), consistent with surveys reporting that *nirS* (iron-containing) generally dominates over *nirK* (copper-containing) in activated sludge microbiomes [51,59]. This is often interpreted as an adaptive preference for iron-based nitrite reduction under iron-replete, low-oxygen activated sludge conditions [59]. The start-up process further amplified this initial *nirS* advantage. The two genotypes occupy distinct ecological niches: *nirS* abundance is more responsive to environmental fluctuations and shows higher nitrite affinity [51,60], whereas *nirK*-type communities are more sensitive to carbon source composition [61]. *nirS*-type communities also possess robust energy-conserving metabolic systems that support survival under stress [62]. In this study, the Carbon Source 2 switch in Stage 4, PAM dosing in Stage 6, and anoxic conversion in Stage 8 imposed exactly such fluctuations, suppressing *nirK* while favoring *nirS*. Meanwhile, the methanol component in Carbon Source 1 has been reported to increase *nirS* diversity while decreasing *nirK* diversity [63]. The observed decline of *nirK* and enrichment of *nirS* therefore represented amplification of a pre-existing advantage rather than de novo competitive replacement. The key DNRA gene *nrfA* showed a fluctuating downward trend, while the ANRA gene *nasA* was upregulated. This trend is consistent with the above-mentioned ammonia-assimilation strategy. ANRA reduces nitrate to ammonium, which is then assimilated through the GS-GOGAT and GDH pathways, forming a nitrate-ammonium-biomass recycling loop that compensates for the limited ammonia supply under low influent NH_4^+-N. DNRA also produces ammonium but releases it to the environment. Therefore, its decline indicated a shift from dissimilatory release toward assimilatory utilization.

To summarize, while methylotrophic denitrification (with *nirS*-type nitrite reductase) dominated the total nitrogen removal, a multi-source nitrogen acquisition network (nitrogen fixation, urea decomposition, ANRA and ammonia assimilation) besides the nitrification pathway was built simultaneously for nitrogen preservation. This multi-layered and carbon-coupled nitrogen metabolic pattern was possibly advantageous for maintaining efficient nitrogen removal and population stability under oligotrophic and anoxic conditions. However, their quantitative contribution to nitrogen removal could not be resolved and therefore should not be over-interpreted. It has been reported that in an artificially constructed simultaneous nitrification-denitrification (SND) consortium, ammonia assimilation accounted for 36.85% of up-regulated nitrogen-metabolism genes, compared with 25.03% for denitrification, yet denitrification remained the functional framework for nitrogen removal [64]. In saline wastewater systems, ammonium assimilation could even exceed nitrification in contribution under certain conditions [65]. Ammonia assimilation has also been shown to operate concurrently with denitrifying phosphorus removal, recovering over 60% of nitrogen as activated sludge while maintaining >80% nitrogen removal [66]. These reports support the coexistence of denitrification with assimilation-based and multi-source nitrogen acquisition routes, but they also show that the relative contribution of assimilation varies widely across systems. In the present study, biomass accumulation as a result of ammonia assimilation during start-up was partially supported by qPCR (Figure 2a) and MLSS measurements (Figure S3), and the semi-quantitative nitrogen balance in Section 3.2 showed that nitrogen discharged via excess sludge accounted for approximately 20.4% of the influent TN load. However, internally stored nitrogen in the system could not be reliably quantified. Hence, the relative contribution of assimilation versus nitrification in NH_4^+-N removal remains unresolved. At the same time, according to the carbon-nitrogen coupled metabolism in Scheme 2, this pathway depended heavily on the continuous supply of methyl compounds in Carbon Source 1, which also explains the previously mentioned stagnation in *Methylotenera* abundance and the transient increase in TN after switching to Carbon Source 2 in Stage 4.

3.8. Engineering Implications for Mobile Platform Regulation

Several operation-level implications can be drawn from this study. First, the continuous supply of composite Carbon Source 1 containing methanol was vital for maintaining *Methylotenera* abundance to achieve stable denitrification, while overdosing may cause carbon slip. Second, PAM dosing should be minimized or carefully avoided since an average net dosage as low as 0.15 mg/L in Stage 6 could possibly exert broad-spectrum microbial inhibition, which immediately inhibited respiratory activity and perhaps exerted a delayed effect, and it coincided with a transient rebound in effluent TN. Third, PAC dosage should also be optimized, because excessive PAC (e.g., net dosage in Stage 7 as high as 58.3 mg/L) could possibly release Al^{3+} and cause a transient pH decrease, both of which resulted in stress to the cell membrane. Fourth, converting an aerobic tank to anoxic operation in Stage 8 stabilized TN removal, but this benefit was accompanied by decreased metabolic activity and DNA integrity, as well as deterioration of floc stability. Fifth, respiratory activity was the most sensitive and immediate indicator of chemical disturbance and may serve as an early-warning signal, whereas membrane integrity, metabolic activity and DNA integrity are more suitable as delayed or endpoint indicators. Finally, while methylotrophic denitrification dominated the total nitrogen-removal pathway, the composite carbon source probably repressed the initial steps of nitrification and thus the contribution of ammonia assimilation should not be ignored for NH_4^+-N removal. Process regulation should therefore focus primarily on denitrification-related levers such as carbon-source quality and redox configuration, with sludge wasting managed accordingly. Nevertheless, these implications are derived from the tested start-up conditions and should be further verified under longer-term and seasonal operation in future work.

4. Conclusions

A 26-day ambient-temperature start-up of the shipborne "Light of Taihu Lake" platform was investigated across eight operation stages to clarify the microbial mechanisms of nitrogen removal from dredged residual water. Under a low influent C/N ratio (average of 1.47), the platform achieved stable performance, with removal efficiencies of 95.6% for NH_4^+-N and 83.8% for TN, and average effluent NH_4^+-N and TN of 0.139 mg/L and 0.757 mg/L, respectively.

The microbial community went through a four-step succession, including environmental selection (Stage 1), function initiation (Stages 2–5), disturbance response (Stage 6), and reconstruction (Stages 7–8). Notably, this succession was driven primarily by process operations, especially PAM dosing and carbon-source switching. During this succession, *Methylotenera* abundance increased from <1% to 34% and became the most abundant classified genus, forming a functionally complementary cooperative network with *Ellin6067* and *Terrimonas* for efficient nitrogen removal. Among the physiological activity indicators, respiratory activity was the most sensitive to process disturbances, whereas membrane integrity, metabolic activity and DNA integrity remained relatively stable.

Metagenomic analysis further demonstrated that methylotrophic denitrification (with nirS-type nitrite reductase) coupled with central carbon and C1 compound metabolism was the core nitrogen-removal pathway. Nitrification was markedly restructured, with ammonia oxidation genes downregulated, whereas the nitrite-oxidizing module remained abundant. In parallel, a multi-source nitrogen acquisition network (nitrogen fixation, urea decomposition, ANRA and ammonia assimilation) supported nitrogen retention and biomass accumulation under oligotrophic and anoxic conditions. These findings advance understanding of microbial adaptation to low C/N ratio environments and provide a theoretical basis for rapid start-up and precise regulation of shipborne mobile residual water treatment platforms.

Supplementary Materials: The following supporting information can be downloaded at: https://www.mdpi.com/article/10.3390/microorganisms14122764/s1, Figure S1: Dosing profiles of carbon sources (a) and conditioning agents (b) during the ambient-temperature start-up phase; Figure S2: COD (a), total phosphorus (TP) (b), pH (c) and turbidity (d) in the influent and effluent during Stages 2–8 of start-up; Figure S3: Mixed Liquor Suspended Solids (MLSS) in the membrane bioreactor tank during Stages 2–8 of start-up.

Author Contributions: J.H.: conceptualization, investigation, methodology, writing—original draft; Y.H.: writing—review and editing, formal analysis, visualization, supervision; J.T.: investigation, formal analysis, data curation; P.H.: methodology; J.Z.: investigation; H.Z.: data curation; W.Z.: Software; G.M.: validation; M.L.: investigation; R.L.: methodology; W.C.: software; B.H.: resources, project administration; H.L.: conceptualization, writing—review and editing, supervision, resources. All authors have read and agreed to the published version of the manuscript.

Funding: This work was supported by the Tianjin Science and Technology Program Project 25YFK-FYS00020 (Research on On-water Treatment Equipment for Dredging Tailwater from Rivers, Lakes and Reservoirs Targeting Class III Surface Water).

Institutional Review Board Statement: Not applicable.

Informed Consent Statement: Not applicable.

Data Availability Statement: We uploaded the 16S rRNA gene amplicon sequences and metagenomic sequences to the NCBI Sequence Read Archive (SRA) under accession number PRJNA1532598 (https://www.ncbi.nlm.nih.gov/bioproject/PRJNA1532598) (accessed on 8 October 2026). All other data were provided in this study.

Acknowledgments: During the preparation of this manuscript/study, the authors used DeepSeek-V4.1-Flash for language polishing, including grammar correction, wording improvement and readability enhancement. The tool was not used for data analysis, interpretation of results or generation of scientific content. The authors have reviewed and edited the output and take full responsibility for the content for this publication.

Conflicts of Interest: Jiayin Huang, Pan He, Jiejun Zhao, Weimin Zhang and Baoan Hu are employees of China Communications (Tianjin) Ecological and Environmental Protection Design and Research Institute Co., Ltd. This company provided the mobile dredged residual water treatment platform used in this study (the "Light of Taihu Lake") and was responsible for its operation, maintenance and process parameter adjustment under the agreed experimental protocol. The specific contributions of the company-affiliated authors are detailed in the Author Contributions section. Beyond these relationships, the company-affiliated authors declare no other financial or non-financial interests. All other authors declare no competing interests.

References

1. Kato, B.E.D.; Morari, P.H.R.; Calixto, G.; Rodrigues, G.L.D.P.; Santarelli, P.H.; Castilho-Noll, M.S.M.; Dos Santos, N.G. A review of current scientific perspectives on the effects of dredging in freshwater environmental restoration. *Water Air Soil Pollut.* **2025**, *236*, 692. [CrossRef]
2. Soetan, O.; Nie, J.; Viteritto, M.; Feng, H. Evaluation of sediment dredging in remediating toxic metal contamination-a systematic review. *Environ. Sci. Pollut. Res.* **2023**, *30*, 69837–69856. [CrossRef] [PubMed]
3. SedNet. Contaminated Sediments in European River Basins 2004. Available online: http://sednet.org/wp-content/uploads/2016/03/Sednet_booklet_final_2.pdf (accessed on 6 March 2026).
4. Safhi, A.E.M.; Pilehvar, S.; Kioumarsi, M. Review of advances and challenges in alkali-activated materials from dredged sediments. *Open Ceram.* **2025**, *23*, 100824. [CrossRef]
5. Lu, C.; Xu, Z.; Zhang, Y.; Dong, B. Rapid and clean dewatering of dredged sediment via coupling of a two-step flocculation and geotextile filtration. *Chem. Eng. J.* **2024**, *480*, 147604. [CrossRef]
6. Chen, Q.; Ran, F.; Wei, Q.; Zheng, X.; Zhao, M.; Liu, S.; Wang, L.; Fan, C. A review on dewatering of dredged sediment in water bodies by flocculation processes. *Water Air Soil Pollut.* **2024**, *235*, 67. [CrossRef]

7. Lu, C.; Xu, Z.; Dong, B. Enhanced residual water quality in the dewatering process of dredged sediment slurry via flocculation: Intrinsic mechanisms of dissolved organic matter removal using cationic flocculants. *Environ. Res.* **2025**, *285*, 122604. [CrossRef] [PubMed]
8. Song, Z.; Zhang, W.; Gao, H.; Wang, D. Comprehensive assessment of flocculation conditioning of dredged sediment using organic polymers: Dredged sediment dewaterability and release of pollutants. *Sci. Total Environ.* **2020**, *739*, 139884. [CrossRef]
9. Ding, A.; Qu, F.; Liang, H.; Guo, S.; Ren, Y.; Xu, G.; Li, G. Effect of adding wood chips on sewage sludge dewatering in a pilot-scale plate-and-frame filter press process. *RSC Adv.* **2014**, *4*, 24762–24768. [CrossRef]
10. Wang, T.; Wang, C.; Liu, D.; Yang, D.; Li, P.; Dong, B. Rapid dewatering and discharge of residual water quality through geotextile filtration coupled with flocculant treatment of contaminated dredged mud. *Environ. Res.* **2025**, *271*, 121032. [CrossRef] [PubMed]
11. Chen, M.; Hur, J. Pre-treatments, characteristics, and biogeochemical dynamics of dissolved organic matter in sediments: A review. *Water Res.* **2015**, *79*, 10–25. [CrossRef] [PubMed]
12. Li, P.; Ye, J.; Zhang, W.; Hu, F.; Guo, Q.; Xu, Z. The blackening process of black-odor water: Substance types determination and crucial roles analysis. *J. Hazard. Mater.* **2023**, *443*, 130295. [CrossRef] [PubMed]
13. Liang, Z.; Fang, W.; Luo, Y.; Lu, Q.; Juneau, P.; He, Z.; Wang, S. Mechanistic insights into organic carbon-driven water blackening and odorization of urban rivers. *J. Hazard. Mater.* **2021**, *405*, 124663. [CrossRef] [PubMed]
14. Zzhu, G.; Kang, L.; Guo, C.; Shen, R.; Cai, Y.; Huang, W.; Luo, J.; Zhang, Y. Two decades changes of ecosystem structure in Lake Taihu: Characteristics and mechanisms. *J. Lake Sci.* **2026**, *38*, 1331–1350. [CrossRef]
15. Yang, Y.; Li, M.; Hu, Z.; Shim, H.; Lin, J.-G.; Li, X.-Y.; Gu, J.-D. Deep insights into the green nitrogen removal by anammox in four full-scale WWTPs treating landfill leachate based on 16S rRNA gene and transcripts by 16S rRNA high-throughput sequencing. *J. Clean. Prod.* **2020**, *276*, 124176. [CrossRef]
16. *GB 3838-2002*; Environmental Quality Standards for Surface Water. Standards Press of China: Beijing, China, 2002.
17. *DB32/1072-2018*; Discharge Standard of Main Water Pollutants for Municipal Wastewater Treatment Plant & Key Industries of Taihu Area. Jiangsu Provincial Department of Environmental Protection: Nanjing, China, 2018.
18. Li, J.; Tabassum, S.; Khan, I. Integrated magnetic flocculation-horizontal tube sedimentation process for treating dredging residual water: Environmental restoration of Wolong Lake. *Environ. Sci. Adv.* **2026**, *5*, 753–771. [CrossRef]
19. CCCC. Exploring the Next Generation Dredging Tool: Light of Taihu Lake. 2025. Available online: https://en.ccc-cltd.cn/xwzx/ywfb/202508/t20250825_222246.html (accessed on 15 August 2026).
20. Sun, C.; Leiknes, T.; Weitzenböck, J.; Thorstensen, B. Development of a biofilm-MBR for shipboard wastewater treatment: The effect of process configuration. *Desalination* **2010**, *250*, 745–750. [CrossRef]
21. Cai, Y.H.; Li, X.; Zaidi, A.A.; Shi, Y.; Zhang, K.; Feng, R.Z.; Lin, A.Q.; Liu, C. Effect of hydraulic retention time on pollutants removal from real ship sewage treatment via a pilot-scale air-lift multilevel circulation membrane bioreactor. *Chemosphere* **2019**, *236*, 124338. [CrossRef] [PubMed]
22. Hao, Y.; Zhang, H.; Zou, H.; Wang, J.; Sun, L.; Cui, M. Pathogen risk control in shipboard domestic wastewater: Current technologies, challenges, and the potential of micro-nanobubbles. *J. Water Process Eng.* **2026**, *90*, 110376. [CrossRef]
23. Kristensen, J.M.; Singleton, C.; Clegg, L.-A.; Petriglieri, F.; Nielsen, P.H. High diversity and functional potential of undescribed "Acidobacteriota" in danish wastewater treatment plants. *Front. Microbiol.* **2021**, *12*, 643950. [CrossRef] [PubMed]
24. Chen, G.; Bai, R.; Zhang, Y.; Zhao, B.; Xiao, Y. Application of metagenomics to biological wastewater treatment. *Sci. Total Environ.* **2022**, *807*, 150737. [CrossRef] [PubMed]
25. Prorot, A.; Eskicioglu, C.; Droste, R.; Dagot, C.; Leprat, P. Assessment of physiological state of microorganisms in activated sludge with flow cytometry: Application for monitoring sludge production minimization. *J. Ind. Microbiol. Biotechnol.* **2008**, *35*, 1261–1268. [CrossRef] [PubMed]
26. Ziglio, G.; Andreottola, G.; Barbesti, S.; Boschetti, G.; Bruni, L.; Foladori, P.; Villa, R. Assessment of activated sludge viability with flow cytometry. *Water Res.* **2002**, *36*, 460–468. [CrossRef] [PubMed]
27. Hashimoto, K.; Marushima, T.; Nakai, S.; Nishijima, W.; Motoshige, H. The dead cell ratio of bacteria in sludge flocs as an indicator of sludge reduction in sludge ozone process. *Biochem. Eng. J.* **2020**, *154*, 107427. [CrossRef]
28. *GB/T 11901-1989*; Water Quality-Determination of Suspended Substance-Gravimetric Method. Standards Press of China: Beijing, China, 1989.
29. *GB/T 15451-2006*; Industrial Circulating Cooling Water-Determination of Total and Composite Alkalinity. Standards Press of China: Beijing, China, 2006.
30. *HJ/T 51-2024*; Water Quality-Determination of Total Salt-Gravimetric Method. Environmental Standard Institute of MEE: Beijing, China, 1999.
31. Cao, R.; Wan, Q.; Xu, X.; Tian, S.; Wu, G.; Wang, J.; Huang, T.; Wen, G. Differentiation of DNA or membrane damage of the cells in disinfection by flow cytometry. *J. Hazard. Mater.* **2022**, *435*, 128924. [CrossRef] [PubMed]
32. Xiao, X.; Han, Z.; Chen, Y.; Liang, X.; Li, H.; Qian, Y. Optimization of FDA-PI method using flow cytometry to measure metabolic activity of the cyanobacteria, Microcystis aeruginosa. *Phys. Chem. Earth* **2011**, *36*, 424–429. [CrossRef]

33. Cappelier, J.M.; Lazaro, B.; Rossero, A.; Fernandezastorga, A.; Federighi, M. Double staining (CTC-DAPI) for detection and enumeration of viable but non-culturable Campylobacter jejuni cells. *Vet. Res.* **1997**, *28*, 547. [PubMed]
34. Cheng, Y.; Wang, C.; Liu, K.; Pan, S. Towards sustainable management of polyacrylamide in soil-water environment: Occurrence, degradation, and risk. *Sci. Total Environ.* **2024**, *926*, 171587. [CrossRef] [PubMed]
35. Fan, X.-J.; Urbain, V.; Qian, Y.; Manem, J. Nitrification and mass balance with a membrane bioreactor for municipal wastewater treatment. *Water Sci. Technol.* **1996**, *34*, 129–136. [CrossRef]
36. Labelle, M.-A.; Dold, P.L.; Gadbois, A.; Déléris, S.; Comeau, Y. Activated Sludge Production Parameters and Nutrient Content of Organic Sludge Components. *Water Environ. Res.* **2017**, *89*, 51–61. [CrossRef] [PubMed]
37. Kalyuhznaya, M.G.; Martens-Habbena, W.; Wang, T.; Hackett, M.; Stolyar, S.M.; Stahl, D.A.; Lidstrom, M.E.; Chistoserdova, L. Methylophilaceae link methanol oxidation to denitrification in freshwater lake sediment as suggested by stable isotope probing and pure culture analysis. *Environ. Microbiol. Rep.* **2009**, *1*, 385–392. [CrossRef] [PubMed]
38. Dan, Q.; Peng, Y.; Wang, B.; Wang, Q.; Sun, T. Side-stream phosphorus famine selectively strengthens glycogen accumulating organisms (GAOs) for advanced nutrient removal in an anaerobic-aerobic-anoxic system. *Chem. Eng. J.* **2021**, *420*, 129554. [CrossRef]
39. Roy, S.; Nirakar, P.; Yong, N.G.H.; Stefan, W. Denitrification kinetics indicates nitrous oxide uptake is unaffected by electron competition in Accumulibacter. *Water Res.* **2021**, *189*, 116557. [CrossRef] [PubMed]
40. Yang, X.; Liao, Y.; Zeng, M.; Qin, Y. Nitrite accumulation performance and microbial community of Algal-Bacterial symbiotic system constructed by *Chlorella* sp. and *Navicula* sp. *Bioresour. Technol.* **2024**, *399*, 130638. [CrossRef] [PubMed]
41. Li, J.; Zuo, X.; Chen, Q.; Lin, Y.; Meng, F. Genome-resolved metagenomic analysis reveals a novel denitrifier with truncated nitrite reduction pathway from the genus SC-I-84. *Water Res.* **2025**, *282*, 123598. [CrossRef] [PubMed]
42. Fu, Y.; Luo, Y.; Tang, C.; Li, Y.; Guggenberger, G.; Xu, J. Succession of the soil bacterial community as resource utilization shifts from plant residues to rhizodeposits. *Soil Biol. Biochem.* **2022**, *173*, 108785. [CrossRef]
43. Gasol, J.M.; Arístegui, J. Cytometric evidence reconciling the toxicity and usefulness of CTC as a marker of bacterial activity. *Aquat. Microb. Ecol.* **2007**, *46*, 71–83. [CrossRef]
44. Brown, L.; Rhead, M.M.; Hill, D.; Bancroft, K.C.C. Qualitative and quantitative studies on the in situ adsorption, degradation and toxicity of acrylamide by the spiking of the waters of two sewage works and a river. *Water Res.* **1982**, *16*, 579–591. [CrossRef]
45. Sriwiriyarat, T.; Madmanang, R. Biodegradation of high acrylamide concentrations in integrated fixed film activated sludge (IFAS) wastewater treatment system. *Biochem. Eng. J.* **2020**, *159*, 107566. [CrossRef]
46. Wu, N.; Zhang, Q.; Wang, H.; Zhang, Y.; Li, M.; Ji, B.; Bao, Y.; Lin, B.; Ding, Y.; He, Q.; et al. Chronic polyaluminum chloride perturbation shaped community assembly patterns: An overlooked mechanism of nitrogen removal inhibition. *Chem. Eng. J.* **2025**, *503*, 158612. [CrossRef]
47. Mustakhimov, I.; Kalyuzhnaya Marina, G.; Lidstrom Mary, E.; Chistoserdova, L. Insights into denitrification in Methylotenera mobilis from denitrification pathway and methanol metabolism mutants. *J. Bacteriol.* **2013**, *195*, 2207–2211. [CrossRef] [PubMed]
48. Liu, T.; He, X.; Jia, G.; Xu, J.; Quan, X.; You, S. Simultaneous nitrification and denitrification process using novel surface-modified suspended carriers for the treatment of real domestic wastewater. *Chemosphere* **2020**, *247*, 125831. [CrossRef] [PubMed]
49. Vadivelu, V.M.; Keller, J.; Yuan, Z. Effect of free ammonia on the respiration and growth processes of an enriched Nitrobacter culture. *Water Res.* **2007**, *41*, 826–834. [CrossRef] [PubMed]
50. Niu, J.; Liu, Y.; Chao, C.; Wu, Y.; Wang, Q.; Zhao, Y. Regulation of microcurrent on carbon and nitrogen metabolism in denitrification under low carbon-to-nitrogen ratio: Optimizing carbon flux distribution. *Bioresour. Technol.* **2025**, *432*, 132668. [CrossRef] [PubMed]
51. Pold, G.; Bonilla-Rosso, G.; Saghaï, A.; Strous, M.; Jones, C.M.; Hallin, S. Phylogenetics and environmental distribution of nitric oxide-forming nitrite reductases reveal their distinct functional and ecological roles. *ISME Commun.* **2024**, *4*, ycae020. [CrossRef] [PubMed]
52. Rubio-Rincón, F.J.; Lopez-Vazquez, C.M.; Welles, L.; van Loosdrecht, M.C.M.; Brdjanovic, D. Cooperation between Candidatus Competibacter and Candidatus Accumulibacter clade I, in denitrification and phosphate removal processes. *Water Res.* **2017**, *120*, 156–164. [CrossRef] [PubMed]
53. Vorholt, J.A.; Chistoserdova, L.; Stolyar, S.M.; Thauer, R.K.; Lidstrom, M.E. Distribution of tetrahydromethanopterin-dependent enzymes in methylotrophic bacteria and phylogeny of methenyl tetrahydromethanopterin cyclohydrolases. *J. Bacteriol.* **1999**, *181*, 5750–5757. [CrossRef] [PubMed]
54. Nayak, D.D.; Marx, C.J. Methylamine utilization via the N-methylglutamate pathway in Methylobacterium extorquens PA1 involves a novel flow of carbon through C1 assimilation and dissimilation pathways. *J. Bacteriol.* **2014**, *196*, 4130–4139. [CrossRef] [PubMed]
55. Cydzik-Kwiatkowska, A.; Wojnowska-Baryla, I. The impact of organic carbon and ammonia load in wastewater on ammonia-oxidizing bacteria community in activated sludge. *Pol. J. Microbiol.* **2008**, *57*, 241–248. [PubMed]

56. Verhamme, D.T.; Prosser, J.I.; Nicol, G.W. Ammonia concentration determines differential growth of ammonia-oxidising archaea and bacteria in soil microcosms. *ISME J.* **2011**, *5*, 1067–1071. [CrossRef] [PubMed]
57. Nogueira, R.; Melo, L.s.F.; Purkhold, U.; Wuertz, S.; Wagner, M. Nitrifying and heterotrophic population dynamics in biofilm reactors: Effects of hydraulic retention time and the presence of organic carbon. *Water Res.* **2002**, *36*, 469–481, Erratum in *Water Res.* **2003**, *37*, 2531. [CrossRef] [PubMed]
58. Chen, J.; Zhang, D.-m.; Jian, S.; Teng, Q.; Chen, K.; Zhou, S.-l.; Kutubu, S.; Jilani, G. Simulated co-substrate threshold manifests steady-state amelioration of coal gasification gray water via synergistic biotransformations in continuous-flow anoxic/oxic system. *J. Water Process Eng.* **2025**, *72*, 107537. [CrossRef]
59. Xie, X.; Chen, L.; Yuan, J.; Zheng, H.; Zhang, L.; Yu, X.; Liu, X.; Wei, C.; Qiu, G. Metagenomic characterization of the metabolism, evolution, and global distribution of Candidatus Accumulibacter members in wastewater treatment plants. *ISME J.* **2025**, *19*, wraf278. [CrossRef] [PubMed]
60. Goberna, M.; Donat, S.; Pérez-Valera, E.; Hallin, S.; Verdú, M. nir gene-based co-occurrence patterns reveal assembly mechanisms of soil denitrifiers in response to fire. *Environ. Microbiol.* **2021**, *23*, 239–251. [CrossRef] [PubMed]
61. Guo, X.; Liang, Y.; Yan, H.; Nian, Y.; Bu, F. Organic composition of starch wastewater steers denitrifying microbiomes for enhanced nitrogen removal. *iScience* **2026**, *29*, 116217. [CrossRef] [PubMed]
62. Ming, Y.; Abdullah Al, M.; Zhang, D.; Zhu, W.; Liu, H.; Cai, L.; Yu, X.; Wu, K.; Niu, M.; Zeng, Q.; et al. Insights into the evolutionary and ecological adaption strategies of nirS- and nirK-type denitrifying communities. *Mol. Ecol.* **2024**, *33*, e17507. [CrossRef] [PubMed]
63. Hallin, S.; Throbäck Ingela, N.; Dicksved, J.; Pell, M. Metabolic Profiles and Genetic Diversity of Denitrifying Communities in Activated Sludge after Addition of Methanol or Ethanol. *Appl. Environ. Microbiol.* **2006**, *72*, 5445–5452. [CrossRef] [PubMed]
64. Ke, X.; Liao, Z.-L.; Yu, H.; Zhang, Y.-C.; Zhou, S.-P.; Xue, Y.-P.; Zheng, Y.-G. Targeted construction of artificial multicellular SND microbial communities and high ammonia-nitrogen wastewater treatment efficiency analysis. *Int. Biodeterior. Biodegrad.* **2025**, *204*, 106153. [CrossRef]
65. Zhang, M.; Zhang, W.; Jiang, Q.; Zhao, C.; Han, F.; Chen, H.; Li, Y.; Zhuge, Y.; Zhou, W. Assimilation overwhelms nitrification in saline wastewater nitrogen removal: From heterotrophic nitrification and aerobic denitrification strains to microbiomes. *Water Res.* **2026**, *288*, 124694. [CrossRef] [PubMed]
66. Zhang, G.; Li, W.; Li, D.; Wang, S.; Lv, L. Integration of ammonium assimilation with denitrifying phosphorus removal for efficient nutrient management in wastewater treatment. *J. Environ. Manag.* **2024**, *353*, 120116. [CrossRef] [PubMed]

Disclaimer/Publisher's Note: The statements, opinions and data contained in all publications are solely those of the individual author(s) and contributor(s) and not of MDPI and/or the editor(s). MDPI and/or the editor(s) disclaim responsibility for any injury to people or property resulting from any ideas, methods, instructions or products referred to in the content.